Geochemistry Geophysics Geosystems G3
AN ELECTRONIC JOURNAL OF THE EARTH SCIENCES
Published by AGU and the Geochemical Society

*Article*
Volume 9, Number 4
9 April 2008
Q04015, doi:10.1029/2007GC001611
ISSN: 1525-2027



# Central Anomaly Magnetization High documentation of crustal accretion along the East Pacific Rise (9°55′–9°25′N)

**Clare M. Williams**

*MIT/WHOI Joint Program in Oceanography, Department of Geology and Geophysics, Woods Hole Oceanographic Institution, Woods Hole, Massachusetts, USA*

*Now at BP Exploration and Operating Co. Ltd., Chertsey Road, Sunbury-on-Thames TW16 7LN, UK (clare.williams@uk.bp.com)*

**Maurice A. Tivey, Hans Schouten, and Daniel J. Fornari**

*Department of Geology and Geophysics, Woods Hole Oceanographic Institution, Woods Hole, Massachusetts 02543, USA*

[1] Near-bottom magnetic data collected along the crest of the East Pacific Rise between 9°55′ and 9°25′N identify the Central Anomaly Magnetization High (CAMH), a geomagnetic anomaly modulated by crustal accretionary processes over timescales of $\sim 10^4$ years. A significant decrease in CAMH amplitude is observed along-axis from north to south, with the steepest gradient between 9°42′ and 9°36′N. The source of this variation is neither a systematic change in geochemistry nor varying paleointensity at the time of lava eruption. Instead, magnetic moment models show that it can be accounted for by an observed ~50% decrease in seismic Layer 2A thickness along-axis. Layer 2A is assumed to be the extrusive volcanic layer, and we propose that this composes most of the magnetic source layer along the ridge axis. The 9°37′N overlapping spreading center (OSC) is located at the southern end of the steep CAMH gradient, and the 9°42′–9°36′N ridge segment is interpreted to be a transition zone in crustal accretion processes, with robust magmatism north of 9°42′N and relatively low magmatism at present south of 9°36′N. The 9°37′N OSC is also the only bathymetric discontinuity associated with a shift in the CAMH peak, which deviates ~0.7 km to the west of the axial summit trough, indicating southward migration of the OSC. CAMH boundaries (defined from the maximum gradients) lie within or overlie the neovolcanic zone (NVZ) boundaries throughout our survey area, implying a systematic relationship between recent volcanic activity and CAMH source. Maximum flow distances and minimum lava dip angles are inferred on the basis of the lateral distance between the NVZ and CAMH boundaries. Lava dip angles average ~14° toward the ridge axis, which agrees well with previous observations and offers a new method for estimating lava dip angles along fast spreading ridges where volcanic sequences are not exposed.

**Components:** 15,391 words, 12 figures, 2 tables.

**Keywords:** East Pacific Rise; magnetic anomalies; mid-ocean ridges; volcanic processes; magnetic source layer.

**Index Terms:** 3035 Marine Geology and Geophysics: Midocean ridge processes; 3005 Marine Geology and Geophysics: Marine magnetics and paleomagnetics (1550); 9355 Geographic Location: Pacific Ocean.

**Received** 17 August 2007; **Revised** 9 October 2007; **Accepted** 5 December 2007; **Published** 9 April 2008.

Williams, C. M., M. A. Tivey, H. Schouten, and D. J. Fornari (2008), Central Anomaly Magnetization High documentation of crustal accretion along the East Pacific Rise (9°55′–9°25′N), *Geochem. Geophys. Geosyst.*, *9*, Q04015, doi:10.1029/2007GC001611.

## 1. Introduction

[2] Accretion of new oceanic crust at mid-ocean ridges (MOR) is a fundamental geological process that involves complex relationships between magma supply and emplacement, which vary spatially and temporally throughout the MOR system. Much of our understanding of oceanic crustal structure and lithology is derived from ophiolite studies [*Cann*, 1974; *Kidd*, 1977] as well as marine seismic surveys, dredged rock samples, shallow crustal drilling and submersible dives, particularly along fault scarps that form tectonic windows into the crust [e.g., *Auzende et al.*, 1989; *Karson*, 1998; *Lagabrielle et al.*, 1998]. Studies of oceanic crust accretion focus frequently on the narrow zone of youngest crust at the spreading axis, known as the neovolcanic zone (NVZ). Magnetic surveys have identified the Central Anomaly Magnetization High (CAMH), a ubiquitous region of high crustal magnetization located at the spreading axis of many MORs, including the East Pacific Rise (EPR) between 8° and 10°N [*Klitgord*, 1976; *Klitgord and Mammerickx*, 1982; *Carbotte and Macdonald*, 1992; *Lee et al.*, 1996; *Schouten et al.*, 1999, 2003]. The CAMH is believed to reflect the presence of young (<10 ka), highly magnetic lavas [*Klitgord*, 1976], which record the recent peak in geomagnetic field intensity [*Gee et al.*, 1996] and document patterns in the distribution of lavas that compose the present-day NVZ. The CAMH is therefore the time-integrated magnetic contribution of the entire magnetic source layer and reflects vertical and temporal properties of the crust at and near the ridge axis (<5 km). Off-axis, as the lower crust cools through its Curie temperature, dikes and gabbros may also contribute to the magnetic source layer. This additional information on three dimensional, time-dependent processes can enhance the interpretation of seafloor observations, particularly along sections of MOR not covered by seismic surveys.

### 1.1. Regional Setting

[3] Our survey area extends between 9°55′N and 9°25′N on the EPR, along the northern section of the ridge bounded by the Clipperton and Siqueiros Transform Faults (TF) (Figure 1a). As with other MORs, the spreading axis along this section is divided into multiple segments by various bathymetric discontinuities [*Macdonald and Fox*, 1983, 1988; *Lonsdale*, 1983; *Macdonald et al.*, 1984, 1987, 1988, 1992; *Haymon et al.*, 1991; *Fornari et al.*, 1998, 2004; *White et al.*, 2006]. These discontinuities offset the ridge axis over a range of scales, from the large 9°03′N overlapping spreading center (OSC) [*Lonsdale*, 1983; *Macdonald and Fox*, 1983], with 8 km offset, to multiple small "devals" (deviations in axial linearity, recognized by *Langmuir et al.* [1986], *Toomey et al.*, 1990, and *Haymon et al.* [1991, 1993]) or "SNOOs" (small nonoverlapping offsets [*Batiza and Margolis*, 1986]) with offsets <0.5 km. The larger discontinuities are thought to represent boundaries between adjacent magmatic systems and are known to migrate along the ridge axis (e.g., the 9°03′N OSC migrates at a rate of ~50 mm/a [*Carbotte and Macdonald*, 1992]) [*Macdonald et al.*, 1992; *Kent et al.*, 1993; *White et al.*, 2002].

[4] Our understanding of lithospheric structure between 8° and 10°N is based on seismic surveys that have identified both upper and lower crustal features. An axial magma chamber (AMC) has been detected ~1.2–2 km beneath the axis in the surveyed area and the continuity of the AMC reflector is disrupted at several locations along-axis (e.g., at 9°17′N and 9°53′N), suggesting possible individual magma systems [*Detrick et al.*, 1987; *Kent et al.*, 1993; *Vera and Diebold*, 1994; *Toomey et al.*, 1994] or locally enhanced mantle melt supply [*Dunn et al.*, 2000]. Above the AMC, in the upper crust, the reflection from the base of seismic Layer 2A is observed to increase in depth from ~0.2 km at the axis to ~0.5 km at 1–2 km off axis [*Christeson et al.*, 1992; *Harding et al.*, 1993; *Kent et al.*, 1993]. Seismic Layer 2A is assumed to be equivalent to the extrusive volcanic layer, or an alteration front located between the base of the extrusive layer and the top of the dike layer [*Christeson et al.*, 2007]. The doubling in Layer 2A thickness is thought to be caused by significant transport and accumulation of lavas off axis due to eruption overflows from the axial summit trough (AST), by efficient transport through networks of lava tubes and channels [*Hooft et al.*, 1996; *Carbotte et al.*, 1997; *Schouten et al.*, 2003], or by off-axis volcanism fed by dikes that are separate from those that feed the EPR axis [*Goldstein et al.*, 1994; *Perfit et al.*, 1994; *Sohn and Sims*, 2005, and references therein]. *Schouten et al.* [1999] show that the thickening of Layer 2A is reflected in the shape of the cross-axis CAMH, indicating that the extrusive lavas of Layer 2A are a significant magnetic source. The center of present magmatic activity is thought to be located at the northern end of our survey area. Indeed, documented eruptions in both 1991 and 2006 between 9°51′ and 46′N [*Haymon et al.*, 1993; *Rubin et al.*, 1994; *Gregg et*

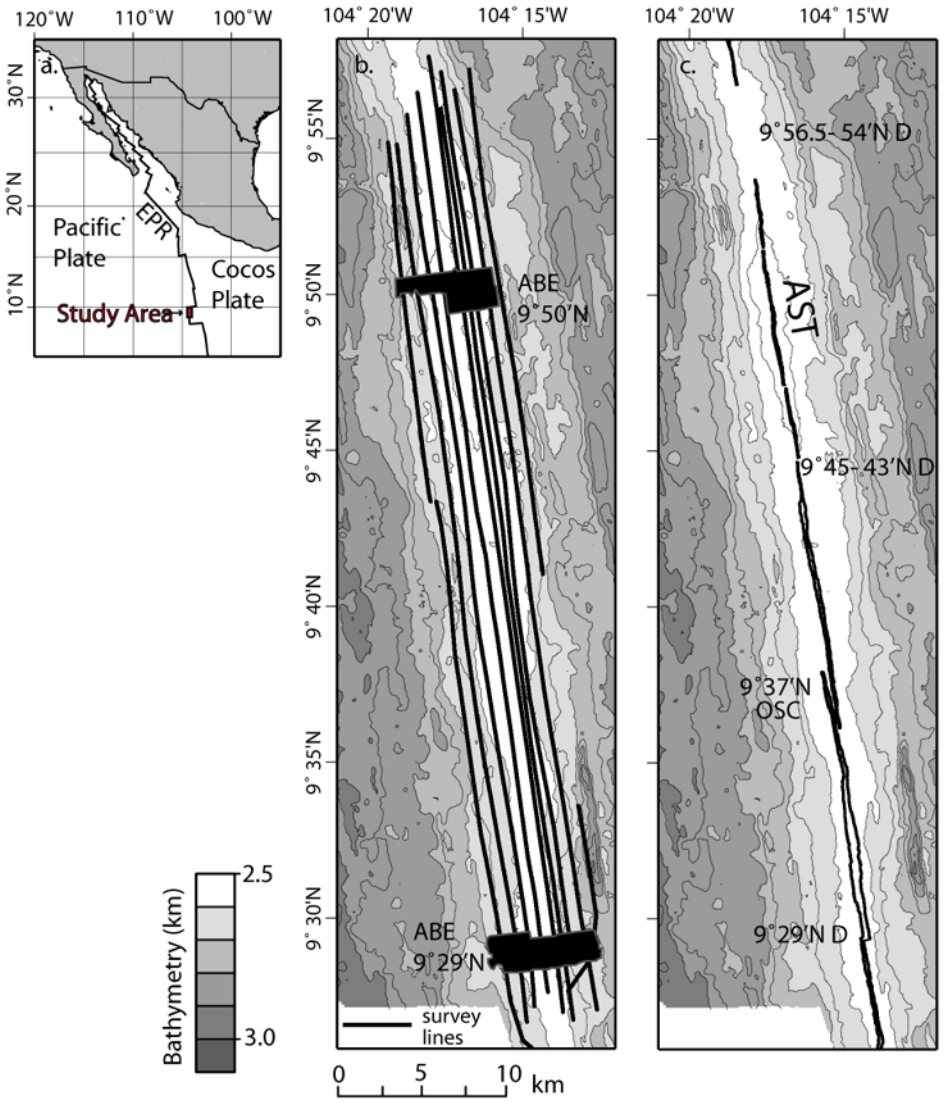


**Figure 1.** (a) Regional location map of the eastern Pacific showing the East Pacific Rise (EPR) and plate boundary between the Pacific and Cocos plates. Our study area, outlined by the red box, is located between 9°55′N and 9°25′N on the EPR. The study area is ~58 km by ~8 km and is centered on the ridge axis. (b) Location map of DSL-120A survey lines (bold black lines) and two Autonomous Benthic Explorer (ABE) survey grids (filled boxes [*Schouten et al.*, 2003]) overlaid on a multibeam bathymetry grid with 50 m contour intervals [*Cochran et al.*, 1999]. (c) Axial Summit Trough (AST, solid black line) [*Fornari et al.*, 2004; *Escartín et al.*, 2007; *Soule et al.*, 2005] represents the present-day spreading axis of the EPR. There are four discontinuities in the AST: the 9°56.5–54′N Discontinuity (D), 9°45–43′N D, 9°37′N OSC, and 9°29′N D.

*al.*, 1996; *Tolstoy et al.*, 2006; *Cowen et al.*, 2007; *Soule et al.*, 2007] and extensive hydrothermal activity in the area [*Haymon et al.*, 1993] support this interpretation.

## 1.2. Magnetic Surveys Between 8° and 10°N

[5] Previous sea surface magnetic studies in the study area identified the CAMH [*Klitgord and Mammerickx*, 1982; *Carbotte and Macdonald*, 1992; *Lee et al.*, 1996] and magnetic discontinuities along the ridge axis that correspond approximately with the location of bathymetric discontinuities at 9°25′N, 9°37′N and 9°46′N [*Lee et al.*, 1996]. However, any correlation between the CAMH and the ridge morphology, and consequently crustal accretion processes, has remained ambiguous because of the inherent low resolution of the sea surface magnetic data used in these studies and the difficulty in mapping the NVZ. As the CAMH

represents a time-integrated signal, a magnetic discontinuity would indicate ridge processes that were stable on timescales of a few thousand to tens of thousands of years [*Macdonald et al.*, 1991; *Carbotte and Macdonald*, 1992; *Lee et al.*, 1996; *White et al.*, 2002]. A correlation between the location of a present-day bathymetric discontinuity and a magnetic discontinuity would provide evidence for the relatively stable position of the ridge discontinuity over these timescales.

[6] The near-bottom magnetic survey that we report on here was conducted between 9°55′ and 9°25′N, during acquisition of side-scan sonar data that covered the ridge axis and flanks out to ~5 km (cruise AT7-4 [*Fornari et al.*, 2004; *Escartín et al.*, 2007; *Soule et al.*, 2005]). The study area encompasses several previous, smaller scale magnetic surveys and the new data provide a regional context for the CAMH. Magnetic data were collected ~100 m above the seafloor using a sensor mounted on the deep-towed DSL-120A vehicle, a 120 kHz side-scan sonar system operated by the National Deep Submergence Facility [e.g., *Scheirer et al.*, 2000, and references therein]. The survey lines were run parallel to the ridge axis at a tow speed of 1.2 kts, with a line spacing of ~0.5 km, and covered an area of ~440 km$^2$ (Figure 1b). Our data set ties together several high-resolution, near-bottom magnetic profiles collected by Alvin at ~5 m altitude [*Schouten et al.*, 1999], and high-density grids collected by the Autonomous Benthic Explorer (ABE) at ~40 m altitude and 40 m line spacing (Figure 1b) [*Schouten et al.*, 2003; *Fornari et al.*, 2004, M. A. Tivey et al., manuscript in preparation, 2008].

[7] Our data set provides a unique opportunity to compare and contrast the CAMH directly with various physical attributes of the NVZ, including the AST and seafloor morphology, which have been interpreted from side-scan data collected concurrently with the magnetic data [*Fornari et al.*, 2004; *Soule et al.*, 2005]. The extent of the NVZ is based on the side-scan acoustic backscatter intensity as outlined by *Escartín et al.* [2007], where acoustically bright seafloor found adjacent to the axial trough is less sedimented and therefore younger in age compared to the less reflective older seafloor. The AST varies in width (<50–400 m) and depth (<5–15 m) [*Fornari et al.*, 1998, 2004] along-axis and is discontinuous at several locations in our survey area (Figure 1c). Four main AST discontinuities have been identified, the largest of which is a right-stepping OSC located between 9°36′ and 38′N (labeled 9°37′N OSC in Figure 1c, ~0.5 km offset) [*Haymon et al.*, 1991; *Macdonald et al.*, 1992; *Smith et al.*, 2001; *White et al.*, 2002]. Establishing the position and character of the CAMH relative to these four discontinuities is important for understanding the stability of small-scale bathymetric discontinuities along fast spreading MORs over time.

[8] In this paper magnetic moment models show an observed decrease in CAMH amplitude along-axis can be explained by variations in seismic Layer 2A thickness alone, implying that the extrusive volcanic layer composes the majority of the magnetic source layer along-axis. A steep gradient in CAMH amplitude between 9°42 and 36′N is interpreted to be a transition zone in ridge crustal accretion processes. The 9°37′N OSC is located at the southern end of the steep gradient and is associated with a magnetic "deviation" of the CAMH peak to the west of the AST. Together, these observations suggest that 9°37′N OSC is a significant ridge discontinuity along this section of the EPR. Finally, the CAMH boundaries lie within or align along the NVZ boundaries throughout the survey area, indicating a relationship between recent volcanic deposits and the CAMH source. The lateral distance between the CAMH and NVZ boundaries is used to interpret flow distances and lava dip angles.

## 2. Methods

[9] Magnetic field data were collected during research cruise AT7-4 aboard the R/V *Atlantis* in 2001 using a 3-axis magnetometer mounted on the DSL-120A side-scan sonar vehicle. Vehicle position was calculated by layback using acoustic travel time for range and bearing, wire out and the ship's position. Vehicle attitude data (pitch, roll, and heading) were recorded at a sampling frequency of 2 Hz and three component magnetic data at a sampling rate of 10 Hz. A calibration turn was executed at ~1000 m depth before the first line of the survey to correct the data for the permanent and induced magnetic fields of the sonar vehicle using the approach of *Isezaki* [1986] and *Korenaga* [1995]. The calibration calculation entails a least squares inversion to minimize the difference between the observed and a predicted field based on the IGRF [*IAGA Division V Working Group*, 2000]. After the calibration correction was applied to the data, the ~3000 nT effect of the vehicle was reduced to a residual of 300 nT relative to the

predicted field. Despite this calibration we also noted a residual heading effect on turns perhaps due to the additional length of tow cable (~2700 m) at tow depth. As a result we applied an additional heading correction by fitting a cosine curve to the total magnetic field data, essentially resulting in a DC-shift for the north versus south oriented tows.

[10] The survey was designed for optimum side-scan images so that multiple closely spaced (~500–800 m) ridge parallel survey lines were acquired. This survey geometry is not optimal for magnetic surveys but we are able to check our data resolution by making a comparison with sea surface and higher-resolution surveys in two areas in order to evaluate the effective resolution limits of the DSL-120A data set. This is discussed in Appendix A. The observed magnetic data were interpolated along the survey lines and resampled to a 1 min sampling frequency, equivalent to a ~40 m along-track data spacing. The non-crustal contribution of the magnetic field was removed from the anomaly by subtracting the IGRF for 2001 [*IAGA Division V Working Group*, 2000]. The resulting residual magnetic anomaly along each track line is shown in Figure 2a. We did not correct the data for diurnal variation because our magnetic anomaly amplitudes are more than an order of magnitude greater than typical diurnal variations at this latitude (note that typical diurnal variations are less than 30 nT [*Lee et al.*, 1996] and the average CAMH amplitude is ~1000 nT cross axis). We checked for the occurrence of magnetic storms at the nearest geomagnetic observatory (Huaycan, Peru). The majority of the survey took place during geomagnetic quiet days with the exception of a magnetic storm on 24–25 November that was at the end of the last line of the survey and it had little to no effect on our data. The along-track residual magnetic anomaly data (Figure 2a) were interpolated into a residual anomaly grid with an anisotropic grid spacing of 0.11 km along-axis and ~0.25 km across axis in order to weight the grid in favor of the higher-resolution data along axis. The residual magnetic anomaly grid was on an uneven plane due to the varying depth of the DSL-120A along each track line. In order to continue the grid to a level datum, and reduce edge effects of the Fast Fourier Transform (FFT) analysis during processing, we increased the area of the residual anomaly grid from ~56 km × 8 km to ~95 km × 73 km by adding data to the edges of the grid from the *Carbotte and Macdonald* [1992] magnetic anomaly grid (original grid spacing 1 km by 1 km). The *Carbotte and Macdonald* [1992] grid is an extensive compilation of sea surface magnetic data from the National Geophysical Data Center data collected between 1967 and 1992 and encompasses the entire segment of the EPR from the Clipperton TF to the Siqueiros TF. The *Carbotte and Macdonald* [1992] grid was continued downward to 2.5 km water depth using a cosine tapered band pass filter with short wavelength cut off of 3 km and long wavelength cut off of 64 km, and resampled to the same grid spacing as the DSL-120A anomaly grid. The residual near-bottom magnetic anomaly grid was then embedded in the center of the resampled *Carbotte and Macdonald* [1992] grid and the two grids combined by minimum curvature interpolation. This new combined residual anomaly grid was then continued upward to both 2.5 km water depth (Figure 2b) and the sea surface using the iterative FFT method of *Guspi* [1987].

[11] The topographic contribution to the magnetic anomaly and both the phase shift and amplitude distortion due to latitude were removed by inverting the data for crustal magnetization, assuming the topography forms the top boundary of a source layer with constant thickness. The *Parker and Huestis* [1974] FFT inversion method was used as adapted by *Macdonald et al.* [1980] for three-dimensional problems. Two multibeam bathymetry grids were combined, in the same way as the *Carbotte and Macdonald* [1992] and near-bottom anomaly grids, to provide bathymetric data over the same spatial area as the residual magnetic anomaly grid. The two multibeam bathymetry grids used were the *Cochran et al.* [1999] grid, covering the area along and near the ridge axis (grid spacing ~0.08 km), and the more spatially extensive grid of *Macdonald et al.* [1992] (grid spacing ~0.3 km). The inversion assumes that the magnetization is uniform with depth and oriented parallel to an axial geocentric dipole (i.e., a declination of 0° and inclination of 32°). A cosine tapered band-pass filter (short wavelength cut-off of 0.5 km and long wavelength cut-off of 45 km) was applied and a constant source layer thickness of 0.25 km assumed. It must be remembered that this layer thickness reflects only the on-axis thickness and that the volcanic layer doubles in thickness within a few kilometers of the axis [*Christeson et al.*, 1992; *Harding et al.*, 1993; *Kent et al.*, 1993], which will also have an effect on the magnetic signal [*Schouten et al.*, 1999]. The oceanic crust in our survey area was accreted during the Brunhes, an interval of normal polarity, there-

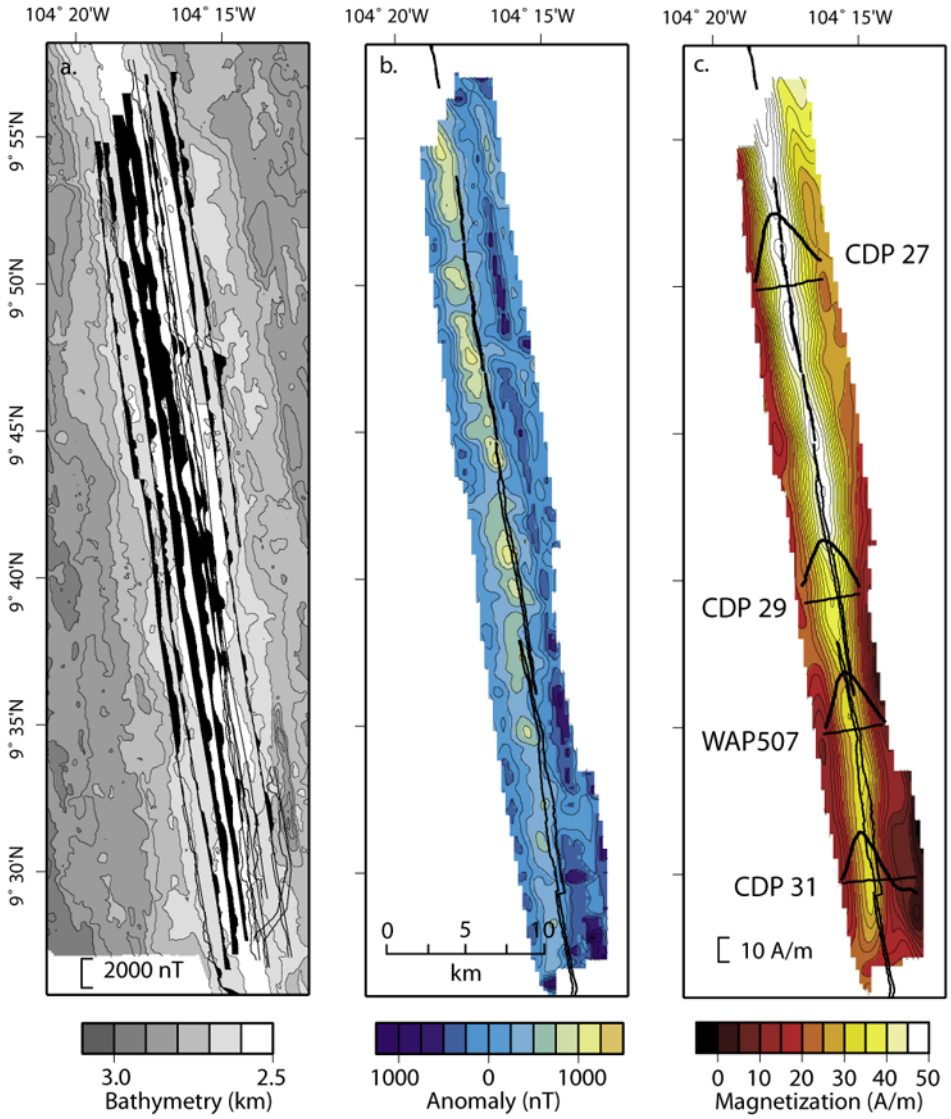


**Figure 2.** (a) Near-bottom residual magnetic anomaly data along the survey lines (positive anomalies are filled). (b) The data are gridded (0.11 km along-axis and 0.25 km across-axis grid spacing) and the residual anomaly grid continued upward to a level plane at 2.5 km water depth using the method of *Guspi* [1987]. (c) The continued grid is inverted for crustal magnetization assuming a constant source layer thickness of 0.25 km. Eighteen times the annihilator are added to the grid to shift the magnetization to all positive values. The inversion results show the Central Anomaly Magnetization High (CAMH) located along the ridge axis. The four CAMH cross-axis profiles shown are located along seismic profiles CDP 27, 29, and 31 [*Harding et al.*, 1993; *Kent et al.*, 1993] and WAP 507 [*Vera and Diebold*, 1994]. The contour interval is 2.5 A/m.

fore all the crustal magnetization results from the inversion should be positively magnetized. We adjusted the magnetization solution to all positive values by adding the annihilator multiplied by a factor. The annihilator is a magnetization distribution that produces no external field when convolved with topography [*Parker and Huestis*, 1974]. For our survey, eighteen times the annihilator was required to shift the crustal magnetization results to all positive values (Figure 2c). No significant change in the pattern of computed magnetization is observed when adding this amount of annihilator, other than shifting the DC-level of the magnetization solution.

[12] A comparison of our inversion results with several previous studies show similar ranges in magnetization intensities for this segment of the EPR away from the 9°03′N OSC, which is likely complicated by high-FeTi lavas and potentially

thicker extrusives at the propagating rift tips [*Bazin et al.*, 2001]. The magnetization range for our data (herein referred to as the near-bottom data) is ~22 A/m. *Lee et al.* [1996] intensities range from 8–16 A/m assuming a source layer thickness of 0.5 km. To a first order, the magnetization magnitude scales linearly with source layer thickness, so that 8–16 A/m would be equivalent to 16 to 32 A/m (16 A/m range) for a 0.25 km thickness. *Carbotte and Macdonald* [1992] studied the entire segment from 8°N–10°30′N and calculated intensities of ~4–10 A/m between 9°25′N and 10°N for a source layer thickness of 1 km, equivalent to 16 to 40 A/m (24 A/m range) for a source layer thickness of 0.25 km.

## 3. Results

[13] Our inversion results show the CAMH morphology is an elongate, linear magnetic high, centered about the ridge axis (Figure 3c). The boundaries of the CAMH are defined by the maximum gradient on each limb (blue solid lines in Figure 3c). Variations exist in both the location of the CAMH boundaries and amplitude and location of the CAMH maximum, or peak. The most significant variation in our study area is a decrease in the CAMH peak amplitude from north to south. The CAMH peak amplitude is relatively high between 9°55 and 43′N (average 47 A/m) and decreases dramatically between 9°42′ and 36′N, to a low of 30 A/m (Figure 3c). The CAMH amplitude then remains relatively low south of 9°36′N. Superimposed on this long wavelength magnetic feature are small scale variations (0.25–1 km) in the CAMH width and location of the CAMH peak. The interpreted backscatter data [*Fornari et al.*, 2004; *Escartín et al.*, 2007; *Soule et al.*, 2005] collected concurrently with the near-bottom magnetic data allows us to compare directly the appearance of the CAMH with the NVZ and present-day AST location.

[14] Overlaying the CAMH and NVZ boundaries shows that the CAMH boundaries lie entirely within or along the NVZ boundaries (Figure 3b). This result suggests a systematic relationship between the source of the CAMH and the young lavas within the NVZ. MOR lavas are often observed to dip toward the ridge axis in cross section exposures within transform faults and other windows into ocean crust [*Kidd*, 1977; *Macdonald et al.*, 1983; *Tivey*, 1996; *Karson et al.*, 2002] although no obvious tilt was observed in the ponded lava drilled in superfast crust at IODP Hole 1256D [*Wilson et al.*, 2006]. Assuming a typical fast spreading MOR that does generate dipping lavas we can use the relative locations of the CAMH and NVZ boundaries to determine lava flow distances and infer lava dip angles (discussed in more detail in section 4.2). The NVZ boundaries are continuous throughout our study area, indicating recent flows on both flanks [*Fornari et al.*, 2004; *Soule et al.*, 2005] (Figure 3a), but they are very irregular compared with the CAMH boundaries. This difference in appearance is expected because the CAMH boundaries are not only band-pass filtered (0.5 km short wavelength cut-off), but they also represent the averaged magnetic signal from the entire magnetic source layer. Both the NVZ and CAMH show along-axis variations in width, the most significant of which is a decrease in width on the eastern flank between 9°48 and 46′N and south of 9°33′N (Figure 3b). These two regions are also associated with deviations in the location of the CAMH maximum or peak away from the AST (herein referred to as magnetic deviations).

[15] The CAMH peak does not overlie the AST trace throughout the study area, but deviates up to 0.7 km onto the ridge flanks (e.g., between 9°50′ and 46′N, 9°45′ and 42′N, and 9°42′ and 36′N and south of 9°33′N, outlined by the grey boxes in Figure 3b). It is interesting to note that three of these four magnetic deviations are to the west of the AST; a result which agrees with the ABE magnetic grids at 9°50′N and 9°29′N (Tivey et al., manuscript in preparation, 2008). The resolution threshold of the near-bottom data is ~0.75 km, on the basis of comparison with the ABE high-resolution grids and multibeam bathymetry (Appendix A, section A2). The two northernmost deviations, between 9°50 and 46′N and 9°45 and 42′N, are well below the 0.75 km resolution threshold and cannot be quantitatively corroborated (Figure 3b). Between 9°42′ and 36′N variations in both the CAMH peak amplitude and location are more striking with the CAMH peak amplitude decreasing dramatically by ~15 A/m over the ~11 km distance (Figure 3c). In addition, the CAMH peak diverges up to ~0.7 km west of the AST as it approaches the 9°37′N OSC from the north (Figure 3b). The CAMH peak overlies the AST again at 9°38′N, where the AST forms the western limb of the 9°37′N OSC, which suggests that the magnetic deviation is associated with the bathymetric discontinuity. South of 9°33′N the CAMH width narrows on the eastern flank and the CAMH peak shifts onto the western flank, ~0.65 km from the AST, resulting in a significant

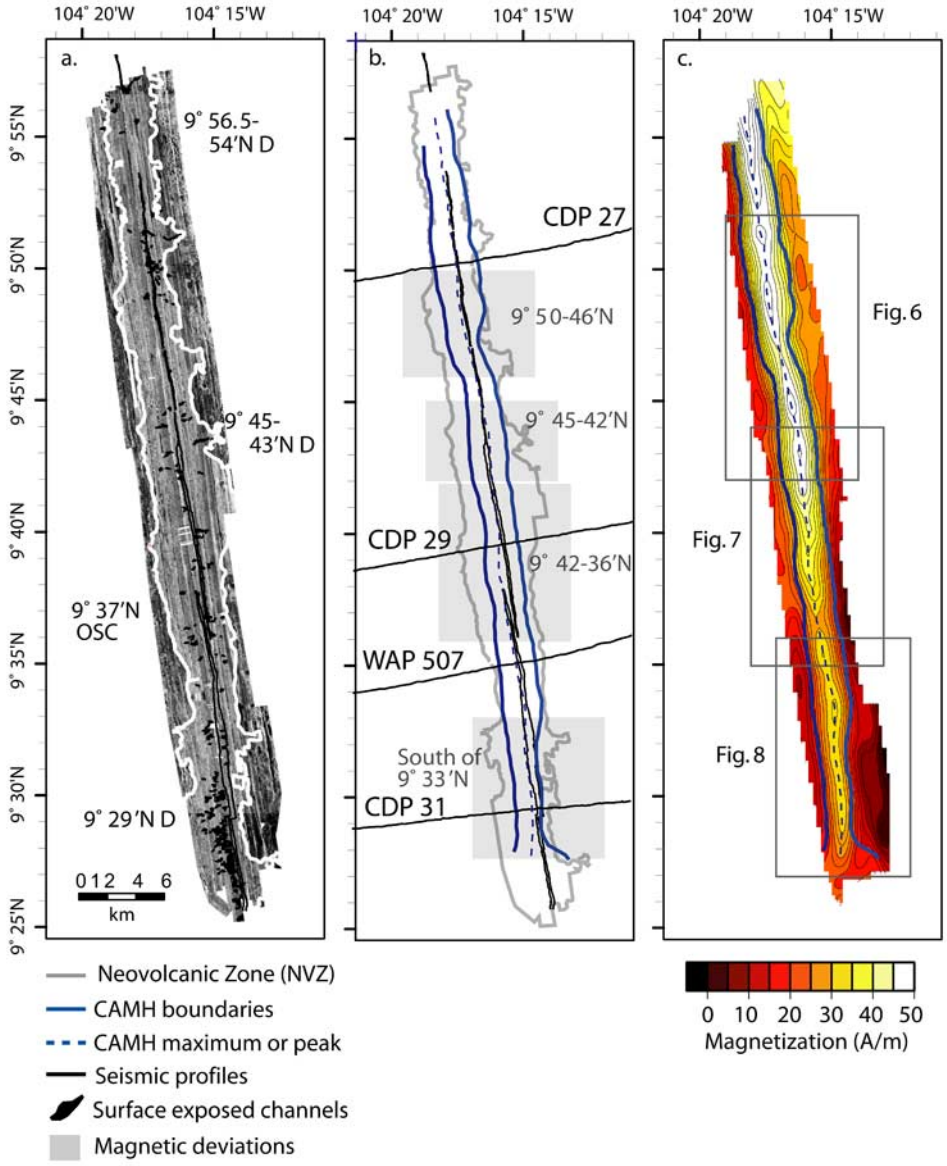


**Figure 3.** (a) Side-scan sonar backscatter data. Areas of high backscatter intensity (bright areas) indicate smooth surfaces and are interpreted as the glassy, sediment-free surface of recent volcanic terrain. Areas of low backscatter intensity (dark areas) indicate rougher surfaces such as pillow lavas and faulted terrain. The off-axis, short black lines represent surface exposed channels [*Soule et al.*, 2005]. The extent of recent volcanism (<10 ka) defined as the neovolcanic zone (NVZ) is shown by the white boundary [*Fornari et al.*, 2004; *Escartín et al.*, 2007]. (b) Comparison of the NVZ boundary (grey line) with the CAMH boundaries and CAMH peak (blue solid and dashed lines, taken from Figure 3c). CDP 27, 29, and 31 and WAP 507 refer to the four seismic profiles. The grey boxes define the four regions where the CAMH peak deviates from the AST. (c) Near-bottom CAMH grid with the CAMH boundaries (solid blue lines) calculated from the maximum cross-axis gradient of the CAMH. The location of the CAMH peak is shown by the blue dashed line. Contour interval is 2.5 nT.

asymmetric location of the CAMH relative to the AST (Figure 3b). The NVZ boundaries are also asymmetric about the ridge axis, with a narrow, irregular eastern boundary and a western boundary extending beyond the survey area (Figure 3b). Both these magnetic deviations (9°42′–36′N and south of 9°33′N) are very close to the near-bottom resolution threshold of 0.75 km.

## 4. Interpretation and Discussion

[16] In the absence of magnetic polarity changes and anomalous topography, magnetic anomalies are generated by two basic mechanisms; either there is more magnetic material, such as a change in volume of the source layer, or the crust is simply more magnetic. The source of the CAMH has been discussed at length in the published literature [*Klitgord*, 1976; *Tivey and Johnson*, 1987; *Gee et al.*, 1996, 2000; *Schouten et al.*, 1999; *Bowles et al.*, 2006]. While rapid alteration [*Gee and Kent*, 1994] and geochemical variations [*Prevot and Lecaille*, 1976] have all been discussed as possible sources of the CAMH, the most widely discussed explanation for the formation and distribution of the CAMH is the recent maximum in geomagnetic intensity and its modulation by crustal accretionary processes in young oceanic crust [*Schouten et al.*, 1999; *Gee et al.*, 2000]. We investigate the relationship between the CAMH and crustal accretion in our study area by integrating our interpretation of the near-bottom data with several other data sets including seismic data, backscatter data and multibeam bathymetry. The resulting combined interpretation allows us to better understand the source of the CAMH and identify variations in its appearance that result from crustal accretionary processes.

### 4.1. Source of Variations in the Along-Axis CAMH Amplitude

[17] The magnitude of the peak CAMH decreases by 15 A/m from north to south in the survey area (Figure 3c). We discuss potential sources of this along-axis magnetic gradient, which can be divided into variations in magnetic properties (magnetization) and volume of the magnetic source layer. At least three processes can affect the magnetic properties of crustal rocks: low-temperature oxidation/alteration of the magnetic minerals, geochemical variability and variations in geomagnetic field intensity. In axial and near-axis locations extrusive basalts are assumed to compose the majority of the magnetic source layer [*Atwater and Mudie*, 1973; *Smith and Banerjee*, 1986; *Pariso and Johnson*, 1991]. The primary carrier of magnetic moment in basalts is titanomagnetite, which is altered to lower magnetic moment titanomaghemite [*Irving*, 1970; *Marshall and Cox*, 1971; *Pariso and Johnson*, 1991]. While systematic and rapid low-temperature alteration has been reported [e.g., *Klitgord*, 1976; *Gee and Kent*, 1994], a more recent study suggests that this is more likely to be a gradual, continuous process which takes place over several millions of years [*Zhou et al.*, 1997]. Therefore, we expect low-temperature alteration to reduce the overall amplitude of magnetic anomalies with age from the ridge axis, but the process is likely too slow to be the primary source of the along-axis gradient in the CAMH.

[18] The second potential source of differences in magnetic properties are geochemical variations and we draw on a large body of published geochemical data from our survey area [e.g., *Batiza and Niu*, 1992; *Perfit et al.*, 1994; *Perfit and Chadwick*, 1998; *Reynolds and Langmuir*, 2000; *Smith et al.*, 2001; *Sims et al.*, 2002; *Soule et al.*, 2005] to evaluate this possibility. Simply stated, the more iron that is present in MORB, the greater the magnetization of the rock. *Gee and Kent* [1997] propose an empirical relationship between FeO content of basalts and their natural remanent magnetization (NRM = 4.44 (FeO) − 25.8). The FeO composition of surface axial basalts in our study area exhibit a trend of increasing FeO weight percent from north to south (M. Perfit, personal communication, 2006) (Figure 4b). This variation is part of a broader trend which shows progressive enrichment in FeO toward the 9°03′N OSC where high-FeTi basalts are found [*Batiza and Niu*, 1992; *Perfit et al.*, 1994]. In this broader context, magnetization also shows higher values toward the 9°03′N OSC as a direct consequence of the high FeTi content in the lavas [e.g., *Carbotte and Macdonald*, 1992; *Sempere et al.*, 1984]. However, for our study area, while FeO content increases from 9.0% at 9°50′N to 10.5% at 9°37′N, equivalent to an NRM increase of ∼6 A/m (assuming the *Gee and Kent* [1997] relationship; Figure 4b), this is opposite to the locally observed decrease in magnetization. We conclude that, although variations in FeO concentrations can affect rock magnetization and we are only sampling surficial rocks, it is unlikely that a systematic variation in geochemical composition is the dominant source of variations in axial magnetization along this section of the EPR and may in fact require greater variation in other potential source mechanisms such as layer thickness.

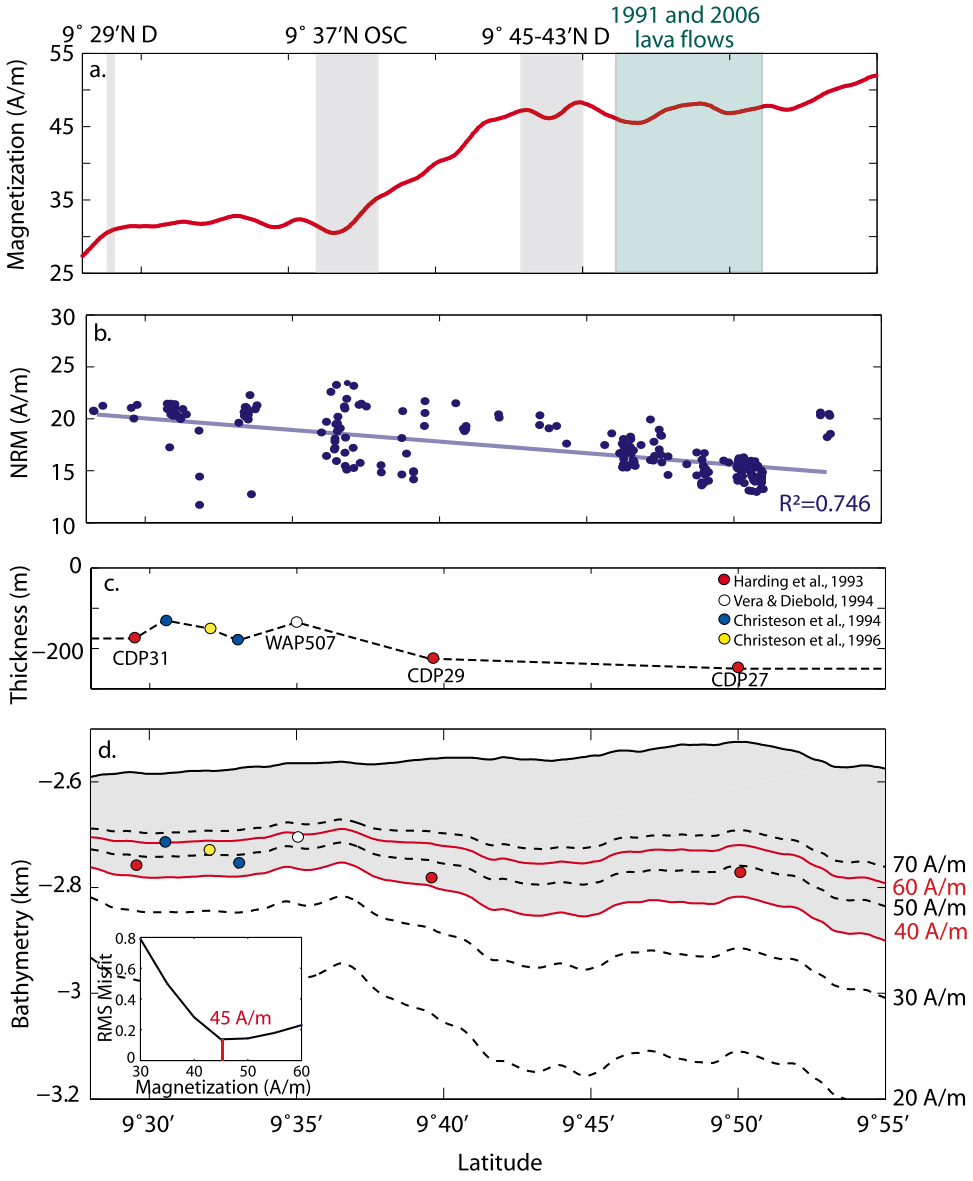


**Figure 4.** (a) Along-axis CAMH peak (assuming a constant source layer thickness of 0.25 km) with the location of the 1991 and 2006 lava flows (green box) and the 9°29′N, 9°37′N, and 9°45′–43′N bathymetric discontinuities (grey boxes). (b) Along-axis NRM calculated from the FeO content of the basalts (M. Perfit, personal communication, 2006) assuming the empirical relationship of *Gee and Kent* [1994], where NRM(A/m) = 4.44(FeO) − 25.8. A running average of the NRM values was calculated, and the linear trend is shown by the solid blue line. The $R^2$ value of 0.746 is statistically low, and this is due to the cluster of high NRM values around 9°53′N. If these data are excluded from the running average calculation, the linear trendline has an $R^2$ value of 0.940. (c) Variation in seismic Layer 2A thickness along the ridge axis. Data from four seismic cross-axis experiments are shown. (d) Model of magnetic source layer thickness required to produce the along-axis variation in the peak CAMH calculated from magnetic moment and a constant magnetization. The model was run for magnetizations of 20–70 A/m in 10 A/m increments, and the resulting source layer thicknesses are shown by the black dashed lines. The red lines encompass the solutions which fall close to the Layer 2A thickness. The best fit solution is a crustal magnetization of 45 A/m, shown by the RMS misfit inset.

[19] A third possible source of magnetization variation are paleointensity fluctuations in Earth's magnetic field. Global changes in the geomagnetic field have been dramatic over the last 10 ka [*Guyodo and Valet*, 1999; *Gee et al.*, 2000; *Yang et al.*, 2000]. On the basis of these records, lavas extruded 5 ka ago would have magnetization intensities approximately one third less than a lava flow extruded 2 ka ago, and lavas extruded today would have magnetization intensities approximately one third less than a lava flow extruded 2 ka ago. Comprehensive analyses of paleointensities from basalt glasses in our study area are presented by *Bowles et al.* [2006]. Their results from both axial and off-axis surface samples show that young lavas (<2 ka) are present at the AST throughout the study area. There are no systematic differences in paleointensity recorded by the glasses that would result in the observed along-axis CAMH gradient. In fact, paleointensities in the 9°30–35′N region are ~7 $\mu$T higher, on average, than those between 9°46 and 50′N; the opposite trend to the along-axis CAMH peak. On the basis of this result, the lavas between 9°30 and 35′N are assumed to be older, which agrees with the interpretation of surface morphology and density of fractures by *Wright et al.* [1995]. It must be kept in mind, however, that these paleointensity data represent the surface lavas only. We are extrapolating these surface data to the entire magnetic source layer. If we discount changes in magnetic properties of the crust as a source of the along-axis variation observed in the peak CAMH, an alternative explanation is a change in magnetic source layer thickness.

[20] The thickness of the magnetic source layer has been found to correlate positively with the seismically defined Layer 2A on the Endeavour segment of the Juan de Fuca Ridge [*Tivey and Johnson*, 1993] and along cross-axis profiles at 9°50′N and 9°31′N on the EPR [*Schouten et al.*, 1999]. *Christeson et al.* [2007] made a direct comparison of geologic and seismologic structure of oceanic crust along the fast spreading EPR crust near Hess Deep and the intermediate spreading Juan de Fuca crust near the Blanco transform fault. They found that while the base of seismic Layer 2A is located at the top of the sheeted dike complex at Hess Deep, it lies within the lava layer at Blanco. *Christeson et al.* [2007] suggest that the Layer 2A reflector may therefore be an alteration boundary rather than a lithologic boundary. However, it is clear that in fast spreading crust, seismic Layer 2A appears to be a good first order estimate of extrusive lava thickness.

[21] Four cross-axis seismic profiles (Figures 2c and 3b; three Common Depth Profiles (CDP) [*Harding et al.*, 1993] and one wide-angle profile (WAP) profile [*Vera and Diebold*, 1994]) and several other shorter profiles (conventional airgun data [*Christeson et al.*, 1996] and refraction study profiles [*Christeson et al.*, 1994]) show that seismic Layer 2A thickness at the axis decreases from north to south (Figure 4c). Seismic Layer 2A has a maximum thickness of ~250 m at 9°50′N and a minimum thickness of ~130 m at 9°31′N. The greatest change in Layer 2A thickness (90 m) is between seismic profiles WAP 507 (9°35′N) and CDP 29 (9°39′N).

[22] The source layer thickness required to produce the along-axis variation in the peak CAMH can be calculated using magnetic moment, which is the product of magnetization intensity and source layer thickness. Our inversion assumes a constant source layer thickness of 0.25 km, which we multiply with the computed magnetization profile (Figure 4a), which includes 18 times the annihilator, to obtain magnetic moment. A series of source layer models are then generated to match this magnetic moment, assuming fixed magnetization values of 20–70 A/m in 10 A/m increments (Figure 4d). The model results show a decrease in source layer thickness from north to south, with the steepest gradient between 9°39′ and 35′N. Increasing the magnetization of the source layer reduces the thickness required to produce the CAMH. Our model results for a crustal magnetization of 45 A/m produces the best fit to the seismic Layer 2A thickness (RMS misfit shown in Figure 4d). This value of crustal magnetization compares well with published NRM values of ~55 A/m for axial lavas at 12°N on the EPR [*Gee and Kent*, 1994].

[23] Our comparison of the magnetic source layer thickness with seismic Layer 2A thickness is limited by the sparseness of the seismic data set. Seven data points are available to constrain Layer 2A thickness, with only two between 9°55 and 35′N (Figure 4c). Our model of the magnetic source layer produces a more detailed picture of the variations in the along-axis source layer thickness and constrains the largest variation to between 9°42 and 36′N. This region coincides with the 9°37′N OSC at its southern end and reflects an along-axis transition zone which begins at 9°42′N and terminates at 9°36′N. In comparison, there is no significant change in magnetic source layer thickness near the magnetic deviation south of 9°33′N or at the two northern bathymetric discon-

tinuities. Our results agree with previous studies which have highlighted the importance of the 9°37′N OSC and suggested that this bathymetric discontinuity represents a boundary between magmatic systems [*Lee et al.*, 1996; *Smith et al.*, 2001]. *Haymon and White* [2004] proposed that ridge segments between discontinuities that offset the ridge 0.5–3 km arise from processes controlling melt supply in the mid-to lower crust, whereas shorter ridge segments between small (<0.5 km) discontinuities are due to upper crustal processes. In light of this, the 9°42–36′N magnetic deviation and transition zone likely results from variations in lower crustal melt supply, which is evident from the changing Layer 2A thickness.

[24] We conclude from our model that the along-axis gradient in the CAMH peak can be well accounted for by variations in magnetic source layer thickness that also correlates well with a similar variation in seismic Layer 2A thickness. We must view this model as one end-member solution, however, as we have noted above that both FeO content and paleointensity considerations could also impact the along-axis signal amplitude. In fact the trend of increasing FeO content to the south infers a slight increase in magnetization, opposite to the gradient we observe. Thus the thickness of the layer may decrease more than predicted with a constant magnetization model. We also note that the predicted average magnetization of 45 A/m, while within the range of reported NRMs for the EPR [*Gee and Kent*, 1994], is significantly more than predicted by FeO content 15–22 A/m (Figure 4b). This may suggest that either the magnetic layer is systematically thicker than modeled, perhaps including the dike section and thereby reducing the overall average layer magnetization required or that factors other than geochemistry are also important, such as grain size and paleointensity. For example, *Johnson and Tivey* [1995] report poor correlation between FeO content and high NRMs from a young axial lava flow on the Coaxial segment.

## 4.2. Comparison of CAMH and NVZ Boundary Locations

[25] The CAMH boundaries lie within or are aligned along the NVZ boundaries throughout our study area (Figure 3b). In general, the CAMH and NVZ boundaries show both the most variability and greatest difference in respective locations on the eastern flank, particularly between 9°42 and 40′N, where networks of channels deposit lavas far from the axis and increase the width of the NVZ beyond our survey area (>3 km, Figure 3a) [*Soule et al.*, 2005; *Garry et al.*, 2006]. In these regions the elongate off-axis flows are not accompanied by an increase in the width of the CAMH, which implies that the contribution these flows make to the computed magnetization is not significant compared with the total magnetic source layer. These flows most likely form a thin carapace over older flows and reflect either a sequence of thin flows not recorded by the CAMH, but preserved in the NVZ boundary, or a single lava flow event. We calculate the minimum thickness of a lava flow required to influence the shape of the CAMH based on the resolution of our data. The largest uncertainty in our data is ∼300 nT, due to the calibration correction for the magnetic effects of the DSL-120A sonar vehicle. Assuming 300 nT is the minimum amplitude anomaly detected, we construct a plane layer model, analogous to a young flow on top of an older flow. Our results show that a flow >17 m thick with a magnetization contrast of 10 A/m between the young and older flows produces an edge anomaly >300 nT. The greater the magnetization contrast between the older and younger flows, the thinner the required flow (Table 1).

**Table 1.** Lava Flow Thickness

| Magnetization Contrast, A/m | Thickness, m |
|---|---|
| 5 | 38 |
| 10 | 17 |
| 25 | 7 |
| 50 | 3 |

[26] Typical magnetization intensities of mid-ocean ridge basalts range from several A/m up to 60 A/m [*Gee and Kent*, 1994; *Sempere et al.*, 1988] and magnetization contrasts of 25 A/m may exist, requiring only a 7 m thick flow to modify the CAMH. However, it is difficult to estimate the flow thickness using this approach without further information on the NRM contrasts between lavas inside and outside the NVZ in our survey area.

[27] The fact that the CAMH boundary is shifted toward the AST and away from the NVZ boundary implies that lava flows dip toward the spreading axis consistent with observations of upper crustal architecture [*Kidd*, 1977; *Macdonald et al.*, 1983; *Tivey*, 1996; *Karson et al.*, 2002]. Lava flows deposited at or near the ridge axis are rafted away

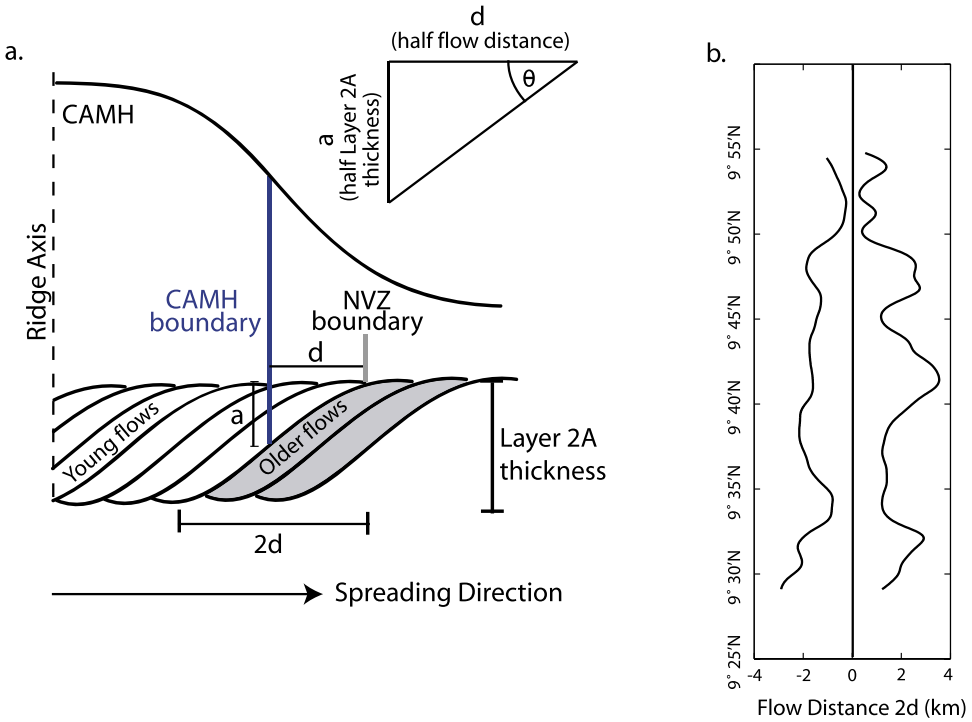


**Figure 5.** (a) Cartoon illustrating the location of the CAMH boundary inside the NVZ due to the dip of lava flows toward the spreading axis. The NVZ and CAMH boundaries are shown by the grey and blue lines, respectively. The distance *d* between the two boundaries represents half the flow distance of the lavas from the spreading axis. The thickness *a* represents half the Layer 2A thickness. We calculate the dip of the lavas along the four seismic profiles where Layer 2A thickness is known. (b) Along-axis variations in the flow distance, 2*d* (these data have been filtered using a 1 km low-pass filter).

during seafloor spreading and the proximal parts of the earlier flows are covered by subsequent flows, resulting in isochrons which dip toward the ridge axis in the upper crust section. A cartoon of this approach is shown in Figure 5a. The lateral distance between the NVZ and CAMH boundaries can be used to calculate lava flow distances and, given an estimate of extrusive layer thickness, infer lava dip angles assuming constant magnetization with depth. We define the maximum lava flow distance as twice the lateral distance between the NVZ and CAMH boundaries (distance 2*d*, Figure 5b). This distance, 2*d*, is the maximum flow distance because the NVZ boundary represents the longest rather than the average flow distance.

[28] In our study area the maximum flow distance (2*d*) is smallest north of 9°50′N and between 9°35 and 33′N (Figure 5b). *Kurras et al.* [2000] mapped in detail the surface morphology of the NVZ on the eastern flank between 9°52 and 49′N. They observed that most flows were deposited <0.5 km from AST, while occasional flows reach 0.5–1.5 km from the axis, similar to the NVZ at 21°N on the EPR [*Macdonald et al.*, 1980]. The relatively short lava flows are reflected in the NVZ, which is narrowest, on average, north of 9°49.5′N (Figure 3a). Possible explanations for the narrow NVZ and small 2*d* values are either shorter lava flows due to reduced magma supply, or disrupted lava deposition where local topography controls the distribution of lava, such as a fault [*Escartín et al.*, 2007]. The 9°50′N region has the shallowest bathymetry, a dome-shaped cross-section and two documented lava flow eruptions in the past 15 years [*Haymon et al.*, 1993; *Tolstoy et al.*, 2006; *Cowen et al.*, 2007] indicating enhanced, rather than reduced, magma supply. Therefore, lava deposition is most likely controlled by local topographic features such as faulting at the surface. Ridge-parallel normal faults can act as barriers, limiting the off-axis extent of lava flows and locally diverting their course along axis [*Escartín et al.*, 2007]. If this situation persists over long periods of time it could change the appearance of the CAMH. *Schouten et al.* [2003] cite a mostly buried normal fault as the source of the linear magnetic anomaly observed along the eastern flank

**Table 2.** Minimum Lava Dip Angles

| Seismic Line | Seismic Line Latitude | Seismic Layer 2A Thickness, m | | Dip Angle,[a] deg | |
|---|---|---|---|---|---|
| | | West Flank | East Flank | West Flank | East Flank |
| CDP 27 | ~9°50′N | 490 | 390 | 41 (±40) | −21[b] (±20) |
| CDP 29 | ~9°40′N | 395 | 420 | 6 (±2) | 9[c] (±1) |
| WAP 507 | ~9°35′N | 210 | 160 | 12 (±18) | 8 (±3) |
| CDP 31 | ~9°30′N | 230 | 185 | 4[c] (±2) | 10 (±2) |

[a] Error estimates are shown in parentheses.
[b] Negative dip angle, i.e., away from the ridge axis.
[c] Not the minimum dip angle as NVZ boundary extends beyond the limit of survey.

in the 9°50′N ABE grid (Figure A2). They propose that the fault restricts off-axis transport of lava flows that originate at the AST and causes ponding of significant volumes of lava. Short flows between 9°35 and 33′N (small 2*d* values, Figure 5b) may also be due to surface faulting. *Escartín et al.* [2007] mapped a large number of surface exposed faults close to the ridge axis in this region. In contrast, areas with large 2*d* values coincide with the regions we interpret to be covered by a single, or multiple thin, elongate flows (e.g., on the eastern flank between 9°42 and 40′N), or long-term asymmetric lava deposition and have fewer observed surface faults (e.g., on the western flank south of 9°33′N).

[29] We can estimate the minimum dip of the lava flows, due to burial by subsequent lava flows, using the 2*d* value and seismic Layer 2A as a proxy for the thickness of the extrusive layer along the four seismic profiles CDP 27, CDP 29, WAP 507 and CDP 31 (Figure 3b and Table 1) [*Schouten and Denham*, 1979; *Karson et al.*, 1992, 2002; *Hooft et al.*, 1996]. The lava dip angle is a minimum because the 2*d* value is the maximum flow distance.

[30] The lava dip angles vary significantly along axis from 4–41°, with the steepest dips at CDP 27 (~9°50′N) and the shallowest at CDP 31 (~9°30′N). Error estimates, defined by maximum and minimum dip angles (shown in parentheses in Table 2) are calculated on the basis of ±50 m accuracy of Layer 2A thickness [*Harding et al.*, 1993] and the width of one grid cell in the near-bottom data (228 m), which defines the accuracy of the flow distance 2*d*. Shallow dip angles (e.g., <10°) have low error estimates compared with the steep dip angles, calculated in areas where the CAMH and NVZ boundaries are located close to each other. The dip angles for profiles CDP 29, WAP 507 and CDP 31 agree very well with the isochrons modeled by *Hooft et al.* [1996]. In their model, the upper extrusives, composed of long flows, have shallow dip angles ranging from 0–15° (compared with 4–12° in this study). *Karson et al.* [2002] also observed lava dip angles that varied from 20–30° in the upper extrusives along fault scarps the Blanco Transform Fault. The steep and negative dip angles at CDP 27 may reflect a change in lava deposition patterns, with shorter flows defined by the NVZ, compared with longer flows in the past (as recorded by the CAMH). Our method for calculating the minimum lava dip angle has widespread application along other fast spreading MORs, where the extrusive lava sequence is not exposed.

### 4.3. Comparison of Magnetic Deviations and Bathymetric Discontinuities

[31] The near-bottom magnetic data provides a regional context for the CAMH and the unique opportunity to compare the CAMH directly with both the present-day AST and NVZ (Figure 3a) that represents recent crustal accretion (<10 ka [*Goldstein et al.*, 1994]), and multibeam bathymetry (Figure 1c), which represents long-term accretion on the ridge equal to the age of the crust (the maximum age of the crust in our survey area is 65 ka, on the basis of a constant spreading rate of 108 mm/a [*Carbotte and Macdonald*, 1992]). We observe a general westward trend of the CAMH peak away from the AST and identify three regions that show significant variations in the CAMH boundaries and peak location relative to the NVZ boundaries and AST (9°48–46′N, 9°42–36′N and south of 9°33′N, Figure 3b). One of the main focuses of our study is to compare the location of present-day bathymetric discontinuities and changes in the appearance of the CAMH (magnetic deviations) to discern if ridge processes have been

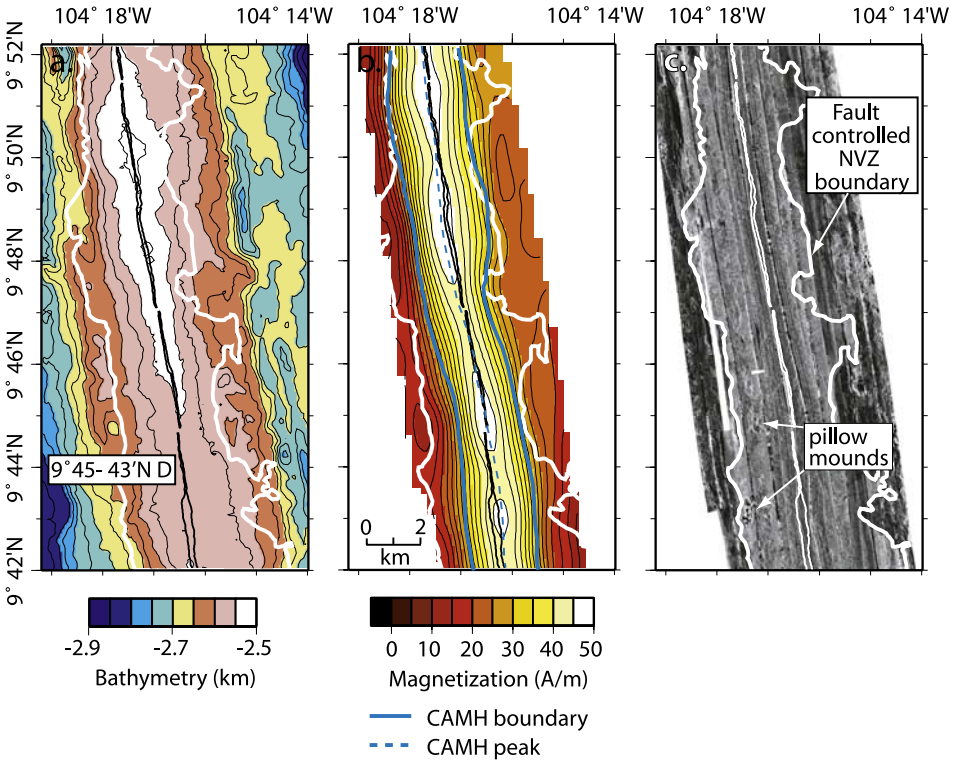


**Figure 6.** The 9°50–43′N region. (a) Multibeam bathymetry with NVZ boundaries (white lines). (b) Near-bottom CAMH magnetization grid with the CAMH boundaries (solid blue lines), CAMH peak (dashed blue line), and NVZ boundaries. (c) Side-scan sonar backscatter data with NVZ boundaries.

stable over magnetic timescales. Of the four main bathymetric discontinuities identified in the AST (Figure 1c), only the 9°37′N OSC appears to be associated clearly with a magnetic deviation. The lack of a magnetic deviation at the other three bathymetric discontinuities may be because they are too young to form a magnetic deviation and/or they migrate over timescales less than $10^3$–$10^4$ a. Alternatively, these discontinuities may produce magnetic deviations that are below the spatial resolution of our data set (~0.75 km). The three regions which show significant variations in CAMH boundary and CAMH peak location are described from north to south below.

[32] In the 9°48–46′N region, the width of the CAMH boundary on the eastern flank decreases by ~0.7 km and coincides with a short wavelength indentation or narrowing of the NVZ at 9°47.5′N (Figure 6c) and a similar narrowing of the 2.6 km contour in the multibeam bathymetry between 9°48 and 46′N (Figure 6a). There is also a small decrease of 4 A/m in the CAMH peak amplitude at 9°47′N (Figure 4a), which agrees well with a decrease in CAMH amplitude observed at 9°46′N in the inversion results of *Lee et al.* [1996] (2.5 A/m for a 0.5 km source layer thickness, which is ~5 A/m for a 0.25 km source layer thickness). We interpret these magnetic and bathymetric features to be the result of disrupted lava deposition by ridge-parallel normal faults, as discussed in section 4.2. However, we cannot identify a specific surface fault that could have caused this disruption in either the backscatter data or still images from near-bottom camera tows in the region (S. Soule, personal communication, 2006). It is possible that part of the fault was covered by the elongate off-axis flow mapped between 9°47 and 46′N on the eastern flank (Figure 3a). A small break in the AST occurs at 9°47′N, but there are no other physical features that explain the disruption. A higher-resolution survey would better define any magnetic deviation of the CAMH peak and possibly identify a bathymetric source for the narrowing of the NVZ and CAMH.

[33] South of 9°40′N, we observe a divergence of the CAMH peak up to 0.7 km to the west of the AST as it approaches the 9°37′N OSC from the north (Figures 7b, 9b, and 10c). The 9°37′N OSC offsets the AST ~0.7 km to the west (the same distance as the magnetic deviation) and the CAMH

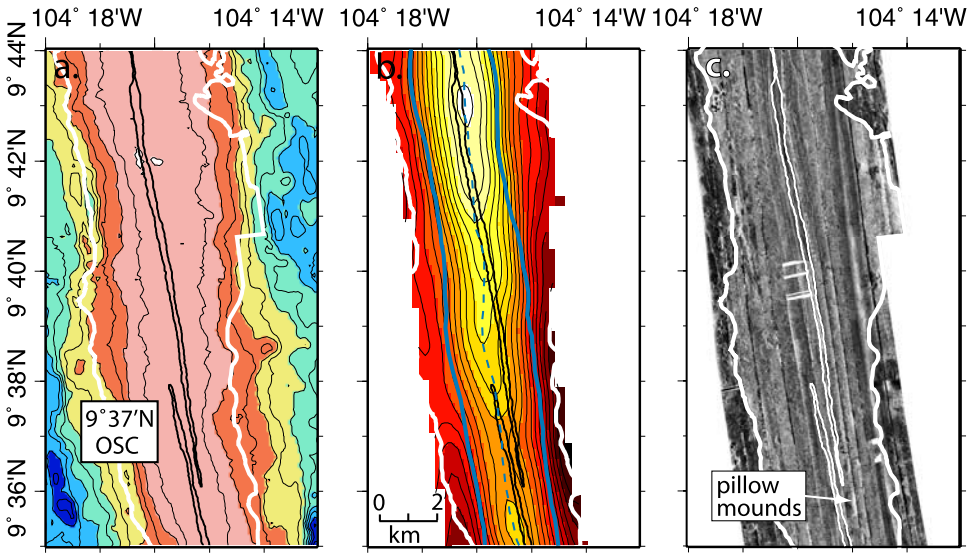


**Figure 7.** The 9°42–36′N region. Plot descriptions and scale bar are the same as those in Figure 6.

peak overlies the AST again at 9°38′N, where the AST forms the western limb of the 9°37′N OSC (Figures 7b and 10c). The NVZ boundaries and multibeam bathymetry both show along-axis changes between 9°42 and 9°36′N. The width of the NVZ and lateral distance of the 2.55–2.6 km contours from the AST are much greater on the eastern flank than the western flank between 9°42 and 39′N (Figures 7a and 7c). This asymmetry in the NVZ and bathymetry is reduced gradually with distance south of 9°39′N to 9°36′N, as the NVZ and the bathymetric contours narrow, but differences in the CAMH gradients persist on both flanks, with steeper gradients to the east compared to the west (Figure 9).

[34] *Lee et al.* [1996] also observe a magnetic deviation or discontinuity around 9°37′N, defined by a decrease in CAMH amplitude of ~2 A/m (equivalent to ~4 A/m for a 0.25 km source layer thickness) and previous studies have identified the 9°37′N OSC as a significant ridge axis discontinuity along this section of the EPR [*Haymon et al.*, 1991; *Batiza and Niu*, 1992; *Wright et al.*, 1995; *Smith et al.*, 2001; *White et al.*, 2002]. *Smith et al.* [2001] proposed that the 9°37′N OSC is propagating to the south on the basis of geochemical, biological and hydrothermal fluid chemistry data, and seafloor morphology at the overlapping limb tips. Their work suggests that the eastern overlapping limb of the OSC is actively propagating to the south, due to a more robust magma supply north of the discontinuity, compared with the western limb, which lacks signs of recent magmatic and hydrothermal activity from the seafloor morphology. The southward propagation of the eastern limb of the OSC follows the same migration direction as the much larger 9°03′N OSC to the south [*Carbotte and Macdonald*, 1992; *Bazin et al.*, 2001]. We interpret the westward divergence of the CAMH peak north of the 9°37′N OSC to be the magnetic expression of this OSC's southward migration. The magnetic deviation from the AST marks the encroaching dominance of the eastern limb over the western limb as it propagates to the south. The backscatter data supports this interpretation with the scalloped edges of sheet lava flows extending throughout the NVZ, implying normal lava deposition, with the exception of an anomalous group of pillow mounds around the terminus of the eastern limb of the 9°37′N OSC (Figure 7c). *White et al.* [2002] frequently observed pillow mounds at the ends of small scale segments (~20 km in length) along the EPR and suggest their presence may indicate an area of disrupted or reduced lava deposition. Wax models used to simulate lava flows show that pillow mounds form at low eruption effusion rates such as those found at the distal ends of lava flows [*Gregg and Fink*, 1995]. We would expect these pillow mounds to be covered by sheet flow lavas in the future, as the eastern limb of the OSC propagates to the south.

[35] The CAMH peak and boundaries south of 9°33′N are asymmetrically located to the west relative to the ridge axis (Figures 8b, 9b, and 10)

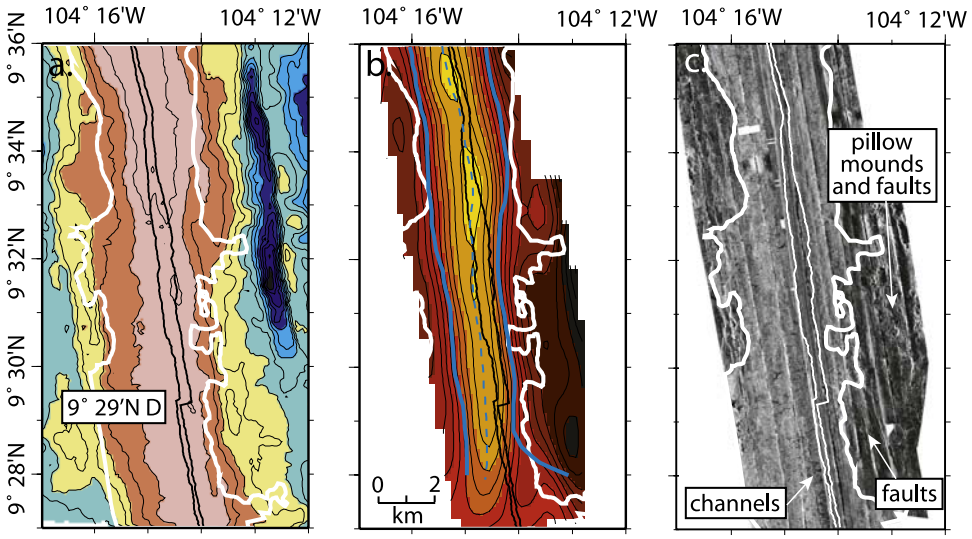


**Figure 8.** Region south of 9°33′N. Plot descriptions and scale bar are the same as those in Figure 6.

and coincide with asymmetric NVZ boundaries (Figure 8c), greater ridge volumes to the west, based on the bathymetric contours (Figure 8a), and thicker seismic Layer 2A [*Harding et al.*, 1993]. The narrowing of the eastern CAMH boundary and more irregular appearance of the eastern NVZ boundary also corresponds with a dramatic increase in the number of surface faults on the eastern flank at 9°33′N [*Escartín et al.*, 2007]. This high density of surface faults continues to the south and is interspersed with pillow mounds (Figure 8c). By comparison, the western flank is dominated by the scalloped edges of sheet lava flows extending from the AST to the edge of the survey. These flows are cut by multiple surface exposed lava channels suggesting significant volcanic deposition in this area (Figure 3a). *Schouten et al.* [1999] interpret the results of an Alvin magnetic profile at 9°31′N as showing the predominantly westward transportation of lava from the AST in contrast to the eastern flank, where numerous faults and hanging basins disrupt lava deposition. The shape and location of the CAMH thus accurately reflects the dominant lava deposition to the west in this region.

## 4.4. Along-Axis Patterns of Lava Deposition

[36] We propose that the variability of the CAMH reflects patterns of lava deposition along the ridge axis and should, therefore, document changes in these patterns. Recent lava distribution patterns (<10 ka) are defined by the NVZ, as opposed to long-term patterns shown by changing ridge morphology in bathymetric surveys. By comparing the appearance of the CAMH with the distribution patterns in both the NVZ and multibeam bathymetry we can determine whether the CAMH has been dominated by short-term patterns, long-term patterns, or both.

[37] On a broad scale there is less variability in the NVZ, CAMH widths and flow distances on the western flank compared with the eastern flank (Figures 10a and 10b). This suggests more consistent recent lava deposition on the western flank throughout our survey area. In contrast, the eastern NVZ boundary shows significant variations, for example, between 9°45 and 38′N the NVZ is at its widest extent and the distance between the NVZ and CAMH boundaries reaches its greatest value (Figures 10a and 10b). The greater variability observed on the eastern flank may be due to the increased number of surface exposed faults on this flank [*Escartín et al.*, 2007]. The western flank appears to be cut by individual east-facing faults that extend long distances along axis (~10 km) and control the western boundary of the NVZ. The eastern flank is very different in appearance, with clusters of shorter (>1 km) west-facing faults that are interspersed with lava covered regions, including elongate flows (Figure 3a). The large number of exposed surface faults on the eastern flank indicates decreased lava deposition or increased tectonic activity, but it is difficult to tell which process occurred first and resulted in the present-day morphology.

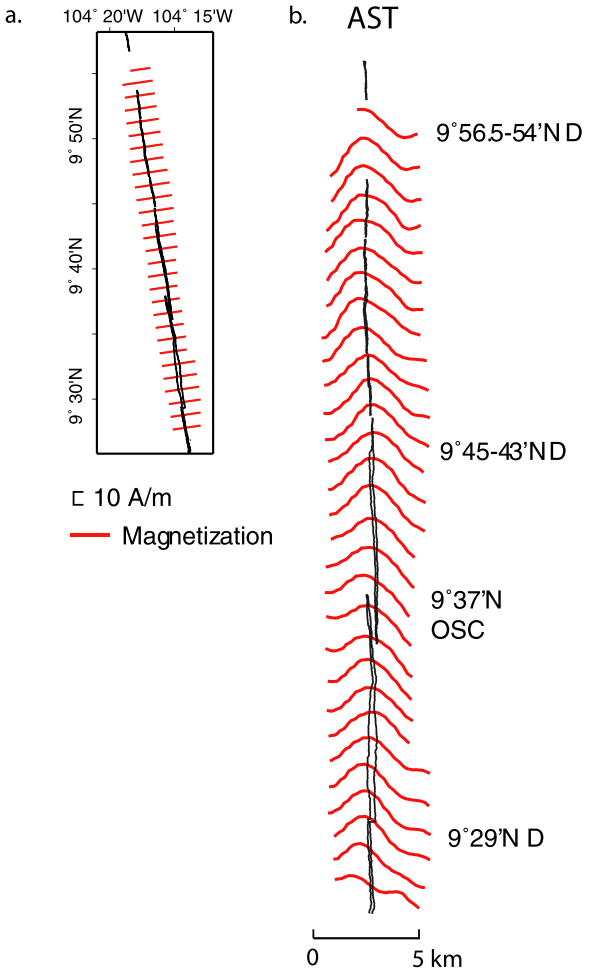


**Figure 9.** (a) Location of cross-axis profiles (approximately every ~1 min) along the ridge axis shown by the red solid lines. (b) b. CAMH profiles and AST have been rotated to vertical.

[38] The EPR bathymetry reflects the long-term complex relationship between magma supply, lava deposition and thermal structure. To quantify long-term lava deposition patters we calculate a proxy for the ridge volume from the cross sectional area of the top 120 m of the ridge axis (Figure 10e) using the multibeam bathymetry data (the calculations are made for each grid cell, ~110 m along axis). Both flanks show varying ridge volumes from north to south (<0.2 $km^2$ to ~0.4 $km^2$), but the eastern flank has greater volumes and more gentle slopes on average (Figures 10e and 10f; the slope is calculated along the same cross-axis profiles as the cross sectional area). The top 120 m of the ridge axis represents <~50 ka old crust, greater than five times the age of the surface flows in the NVZ. In general, the ridge volume shows significant along-axis variations on both flanks, which differs from the CAMH and NVZ boundaries that show more variation on the eastern flank. However, there is a correlation between reduced ridge volumes on the eastern flank and the two regions where the eastern CAMH narrows between 9°49 and 46′N and 9°32 and 28′N (Figures 10a and 10e, indicated by the light blue boxes). The ridge volumes also become asymmetric to the west in the region south of 9°33′N, similar to the CAMH and NVZ boundaries. These areas of disrupted lava deposition are therefore interpreted as being long-lived features (up to ~50 ka) that have modified the shape of the CAMH. Other correlations between the CAMH boundary location and changing ridge volumes are very subtle and we are limited by the resolution of our data set. In summary, the CAMH reflects several regions of long-lived disruptions in lava deposition identified in the bathymetric data (between 9°49 and 47′N and 9°32 and 29′N, Figure 10e). It has also been modified by more recent patterns of lava deposition, as defined by the NVZ (Figure 10a), which shows more consistent lava deposition on to the western flank and the importance of ridge-parallel normal faults in controlling the location of lava deposition.

## 5. Conclusions

[39] We have conducted a detailed study of the CAMH between 9°55′N and 9°25′N on the EPR. The study focuses on identifying the sources of variations in the CAMH and linking these variations to crustal accretion patterns. The process of crustal accretion modifies the shape of the CAMH by controlling the thickness of the magnetic source layer and the deposition of young, highly magnetic lavas. We make the following conclusions:

[40] 1. The most significant magnetic feature in our survey area is an along-axis gradient in the CAMH peak amplitude between 9°42 and 36′N, where the calculated crustal magnetization decreases by ~15 A/m from north to south. This gradient lies within a regional southerly increase in magnetization along axis due to progressive enrichment in FeO toward the 9°03′N OSC where high-FeTi basalts are found. Indeed both the geochemistry and paleointensity variations in our study area suggest gradually increasing magnetization to the south and are therefore discounted as the source of the gradient in our survey area. We propose that variations in magnetic source layer thickness can account for the observed gradient. Our magnetic moment model shows that a source layer with a magnetization of 45 A/m has approximately the

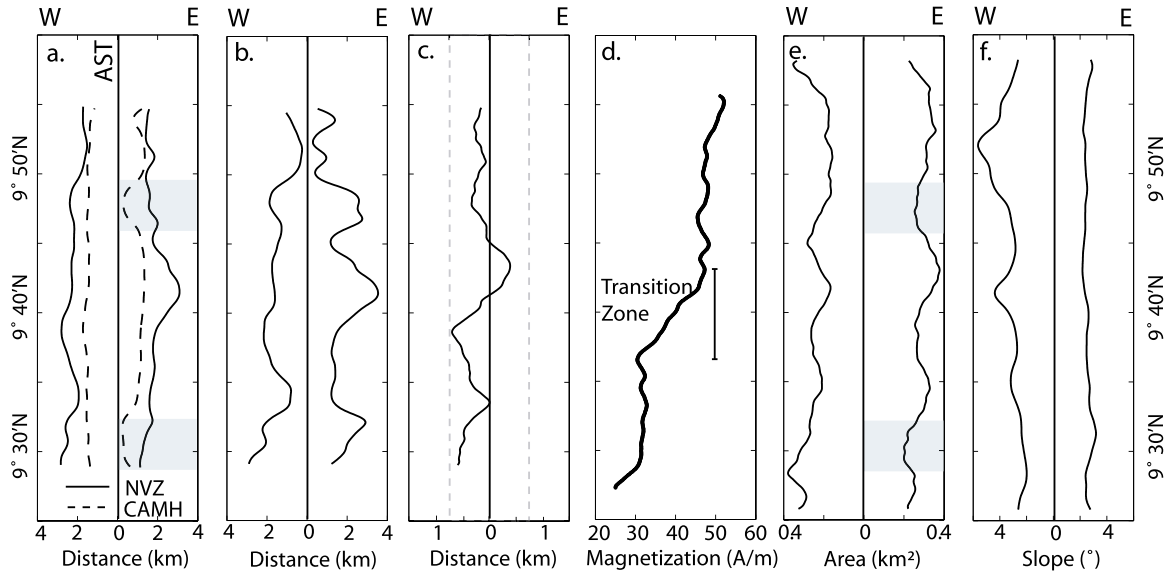


**Figure 10.** Along-axis variations in ridge properties; all data have been filtered using a 1 km low-pass filter, and the zero line on the *x* axis represents the AST. (a) NVZ (solid lines) and CAMH (dashed lines) boundary widths. The light blue boxes coincide with regions of low ridge volume on the eastern flank (Figure 10e). (b) Flow distance 2*d* (twice the distance between the NVZ and CAMH boundaries). (c) Along-axis CAMH peak location relative to the AST. The resolution threshold of the data set, 0.75 km, is shown by the grey dashed lines. (d) Amplitude of along-axis CAMH peak. (e) The cross-sectional area on both ridge flanks calculated from the top 120 m of the ridge and used as a proxy for ridge volume. The light blue boxes indicate regions of low ridge volume on the eastern flank. (f) Cross-axis slope calculated from the average gradient of the top 120 m of the ridge.

same thickness as the measured seismic Layer 2A thickness. Assuming seismic Layer 2A is a proxy for extrusive lava layer in fast-spread crust [*Christeson et al.*, 2007], the peak CAMH gradient can be accounted for by a 50% decrease in extrusive lava layer thickness along axis (from 250 m to 125 m). The 9°37′N OSC coincides with the southern end of the CAMH gradient and we interpret the section of ridge between 9°42 and 36′N to be a transition zone in crustal accretion processes, with a robust magmatic segment north of 9°42′N and a relatively less robust segment south of 9°36′N.

[41] 2. The CAMH boundaries lie entirely within or along the boundary of the neovolcanic zone (NVZ), as defined by acoustically bright seafloor in the backscatter data, suggesting a systematic relationship between the CAMH source and sequences of young lava flows that make up the NVZ. The CAMH boundaries lie within the NVZ boundaries, providing further evidence that the lava flows dip toward the axis. The minimum lava flow dip angles, calculated from the difference in boundary locations and Layer 2A thickness, agree well with both crustal accretion models [*Hooft et al.*, 1996] and observations [*Karson et al.*, 2002], and provides an alternative method to estimate lava dip angles along fast spreading ridges where the extrusive volcanic sequence is not exposed. Occasional elongate flows (e.g., on the eastern flank between 9°42 and 40′N) that deposit lavas up to 3 km from the AST form thin carapaces over older seafloor and do not have enough volume to contribute to the CAMH and thus do not affect its width or shape.

[42] 3. The 9°37′N OSC is the only bathymetric discontinuity that has a magnetic deviation associated with it within the resolution of our data. Approaching the OSC from the north, the CAMH peak shifts from the AST to the western limb of the OSC, reflecting southward migration of the bathymetric discontinuity. These results, combined with the along-axis gradient in CAMH amplitude that terminates near the 9°37′N OSC, indicate that this is a significant ridge discontinuity along this section of the EPR. Magnetic deviations associated with other bathymetric discontinuities may exist but are below the resolution of our magnetic data.

[43] 4. Finally, the correlation between morphological features and variations in the CAMH appear-

ance show that the CAMH, when mapped using near-bottom data, documents crustal accretion processes over timescales of $\sim 10^4$ years. The CAMH reflects both long-term patterns in lava deposition ($\sim$50 ka), defined by the multibeam bathymetry, and short-term patterns, defined by the NVZ (<10 ka). Long-term patterns include disrupted lava deposition on the eastern flank due to ridge-parallel surface faults, while recent patterns show increased lava deposition onto the western flank. The prominent east–west asymmetry in crustal accretion history as documented by the NVZ, multibeam bathymetry and the overlying CAMH may reflect a more fundamental asymmetry in mantle upwelling and ridge migration processes.

## Appendix A: Data Resolution Comparison

[44] A comparison of the near-bottom magnetic data with other magnetic data sets of varying resolution and spatial extent in our survey area provides a unique opportunity to test the quality and resolution of the near-bottom data. This comparison also allows us to address the issue of resolution versus area of surveyed seafloor when designing these types of experiments. The magnetic data sets used for the comparison are sea-surface data [*Carbotte and Macdonald*, 1992], and two high-resolution ABE grids collected at 9°50′ and 9°29′N (Tivey et al., manuscript in preparation, 2008).

### A1. Sea Surface Data

[45] The sea surface CAMH of *Carbotte and Macdonald* [1992] and the near-bottom CAMH, continued to the sea surface, are very similar in their general appearance (Figure A1). The Carbotte and Macdonald magnetic data were processed using the same approach as the near-bottom data (see *Carbotte and Macdonald* [1992] for the location of survey lines). The inversion results show a broad lineated CAMH, with the maximum or peak in amplitude located slightly west of the AST ($\sim$300 m). In general, the amplitude of the CAMH decreases from north to south with three discrete highs located at 9°48′N, 9°41.5′N and 9°32.5′N (Figure A1a). When comparing the Carbotte and Macdonald sea surface CAMH with the near-bottom CAMH (Figure A1b), the latter has higher resolution than the Carbotte and Macdonald CAMH. As expected the overall appearance of the two CAMHs anomaly patterns compare well. The near-bottom CAMH is more symmetric about

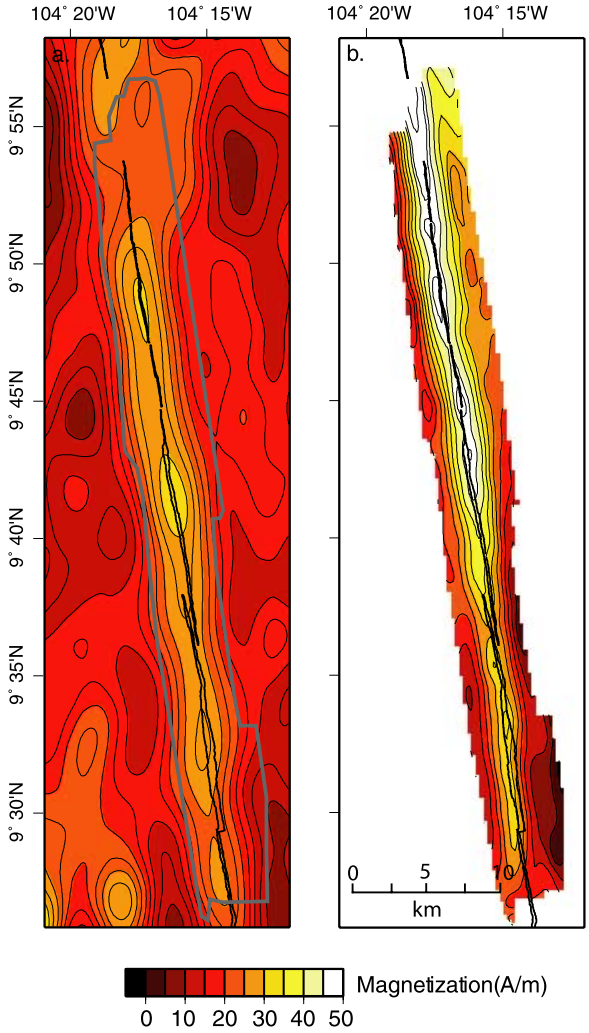


**Figure A1.** A comparison of a sea surface inversion grid with the near-bottom inversion results. (a) Sea surface magnetic grid of *Carbotte and Macdonald* [1992] inverted for a constant source layer thickness of 0.25 km. The area of the DSL-120A survey is shown by the grey outline. (b) The near-bottom inversion results (same as Figure 2c). Eighteen times the annihilator has been added to both grids.

the AST but there are peaks in amplitude at the same locations as the Carbotte and Macdonald CAMH. The near-bottom CAMH better defines the CAMH, with steeper gradients and higher amplitudes, and provides more information about along- and across-axis variations over short spatial scales (<2 km).

### A2. Near-Bottom ABE Data

[46] The resolution of two ABE magnetic grids in our survey area is much greater than the near-bottom magnetic data; but similar wavelength

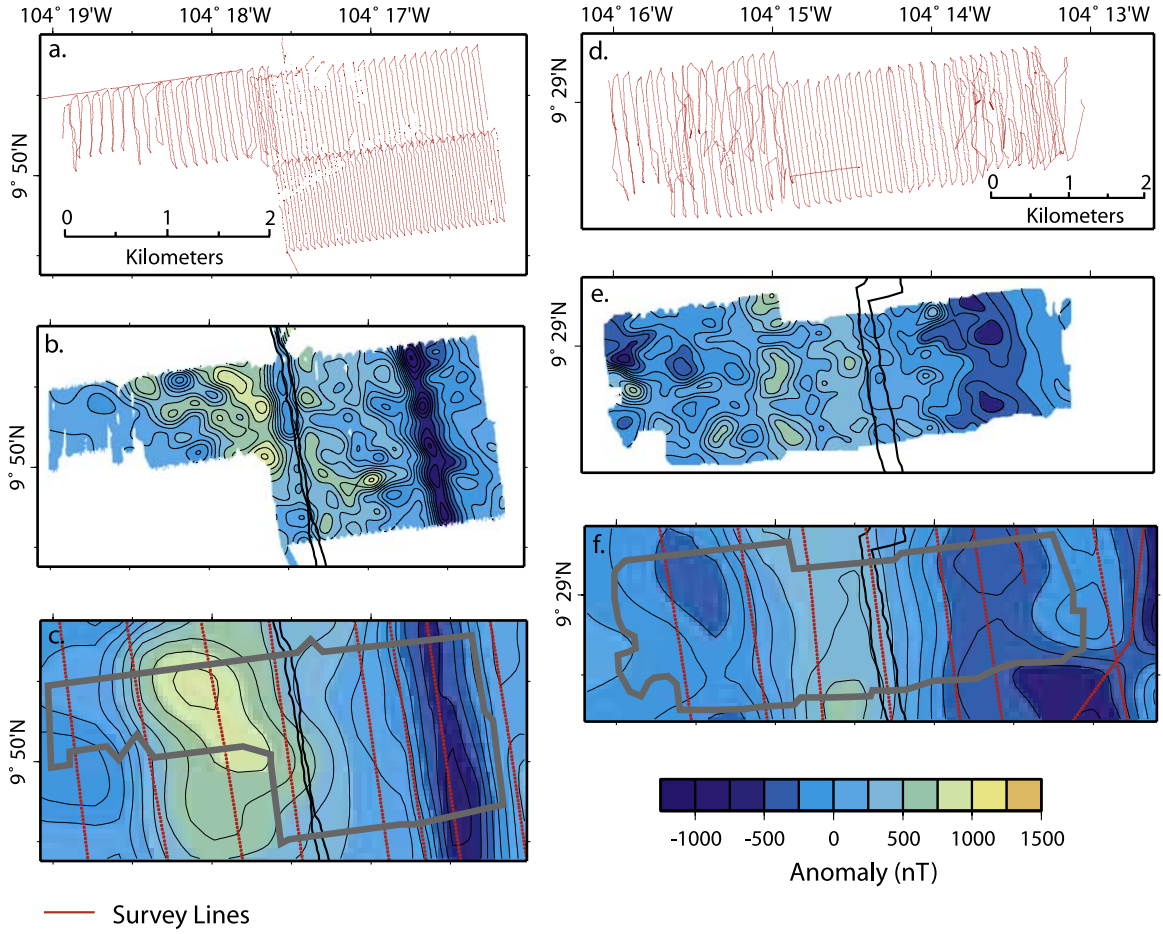


**Figure A2.** A comparison of two high-resolution ABE magnetic grids at 9°50′N and 9°29′N with the DSL-120A grid. (a) Track lines of the ABE grid at 9°50′N (line spacing <40 m). (b) The ABE residual anomaly grid continued upward to 2.5 km water depth [*Schouten et al.*, 2003]. The boundaries of the AST are shown by the bold black line. (c) Near-bottom residual anomaly grid continued upward to 2.5 km water depth. The area of the ABE grid is outlined by the grey solid line. The red dots are data points along the DSL-120A survey lines. (d) Track lines of the ABE grid at 9°29′N. (e) The ABE residual anomaly grid continued upward to 2.5 km water depth. (f) Near-bottom residual anomaly grid continued upward to 2.5 km water depth. The contour interval for all the grids in Figure A2 is 125 nT.

(>0.75 km) magnetic features are observed in both data sets (Figure A2). The two spatially dense ABE magnetic data grids were acquired at 9°50′N and 9°29′N in 2001 (cruise AT7-4, Figure 1b) using a 3-axis magnetometer, mounted on the autonomous vehicle ABE [*Yoerger et al.*, 1996; *Schouten et al.*, 2003; Tivey et al., manuscript in preparation, 2008]. The ABE residual magnetic anomaly grids were continued upward to ~2.5 km water depth for direct comparison with the near-bottom residual magnetic anomaly at 2.5 km water depth. At this time we compare only patterns in the overall anomaly and not anomaly amplitudes.

[47] The ABE 9°50′N magnetic anomaly grid shows that the CAMH has a double peak across the axis, with the intermediate low centered on the AST (Figure A2b). The peak on the western flank has greater amplitude and is located ~0.5 km west of the AST. The most striking magnetic feature in the ABE grid is the steep gradient and linear appearance of the magnetic low that defines the eastern edge of the CAMH, ~1.5 km from the axis (Figure A2b). The eastern edge of the CAMH in the near-bottom data shows the same steep gradient and linear character as the ABE data (Figure A2c). This is a feature that is not well resolved by the sea-surface data. The near-bottom CAMH is very broad with the maximum or peak offset to the west by ~1 km. More near-bottom survey lines close to the AST would be required to resolve a double peak and intermediate low at the AST, as observed in the ABE grid (Figure A2b). There appears to be a correlation between the ABE CAMH and sea-floor morphology, implying that the shape of the

CAMH reflects recent patterns of crustal accretion and may be able to resolve features ~0.25 km in size, on the basis of the dimensions of lava flow fronts identified in the backscatter data [see *Schouten et al.*, 2003]. In contrast to the ABE resolution limit, the near-bottom data is able to resolve features ~0.75 km in size (such as the linear eastern edge of the anomaly).

[48] In the ABE magnetic anomaly grid at 9°29′N, the CAMH is double-peaked with both peaks located asymmetrically on the western flank, at 0.5 and 1 km west of the AST (Figure A2e). The eastern edge of the CAMH has an irregular appearance (unlike the linear feature in the 9°50′N grid). The near-bottom CAMH at 9°29′N also has the same asymmetric nature but resolves only one magnetic high ~0.75 km west of the AST (Figure A2f). Other major features of the near-bottom magnetic anomaly compare well with the ABE data. As in the 9°50′N area, we believe that near-bottom data are able to resolve features on a scale of ~0.75 km.

[49] In summary, our comparison of the near-bottom magnetic data with the sea-surface data and ABE magnetic data at 9°50′N and 9°29′N show that the near-bottom magnetic survey is a valuable data set which allows for extrapolation of magnetic data between the two ABE grids along this section of the EPR. The near-bottom magnetic data provide a high-quality, albeit somewhat low-pass filtered version of the magnetic character of the spreading center.

## Acknowledgments

[50] The authors would like to thank the captain and crew of the R/V *Atlantis* and the Nation Deep Submergence Facility operations, including DSL-120A group. We would also like to thank Mike Perfit and Ian Ridley for access to their geochemical data sets and Johnson Cann, Javier Escartín, and Adam Soule for their assistance and insightful contributions. This manuscript benefited by constructive reviews from John Tarduno, Suzanne Carbotte, Jerome Dyment, and Ken Macdonald. The research project was funded by National Science Foundation under grants OCE-9819261 and OCE-0096468.

## References

Atwater, T., and J. D. Mudie (1973), A detailed near-bottom geophysical study of the Gorda Rise, *J. Geophys. Res.*, *78*, 8865–8886.

Auzende, J.-M., D. Bideau, E. Bonatti, M. Cannat, J. Honnorez, Y. Lagabrielle, J. Malavieille, V. Mamaloukas-Frangoulis, and C. Mevel (1989), Direct observation of a section through slow-spreading oceanic crust, *Nature*, *337*, 726–729.

Batiza, R., and S. H. Margolis (1986), A model for the origin of small non overlapping offsets (SNOOs) of the East Pacific Rise, *Nature*, *320*, 439–441.

Batiza, R., and Y. Niu (1992), Petrology and magma chamber processes at the East Pacific Rise ~9°30′N, *J. Geophys. Res.*, *97*, 6779–6797.

Bazin, S., et al. (2001), Three-dimensional shallow crustal emplacement at the 9°03′N overlapping spreading center on the East Pacific Rise: Correlations between magnetization and tomographic images, *J. Geophys. Res.*, *106*, 16,101–16,117.

Bowles, J., J. S. Gee, D. V. Kent, M. R. Perfit, S. A. Soule, and D. J. Fornari (2006), Paleointensity applications to timing and extent of eruptive activity, 9°–10°N East Pacific Rise, *Geochem. Geophys. Geosyst.*, *7*, Q06006, doi:10.1029/2005GC001141.

Cann, J. R. (1974), A model for oceanic crustal structure developed, *Geophys. J R. Astron. Soc.*, *39*, 169–187.

Carbotte, S., and K. C. Macdonald (1992), East Pacific Rise 8°–10°30′N: Evolution of ridge segments and discontinuities from SeaMARC II and three-dimensional magnetic studies, *J. Geophys. Res.*, *97*, 6959–6982.

Carbotte, S. M., J. C. Mutter, and L. Xu (1997), Contribution of volcanism and tectonism to axial and flank morphology of the southern EPR, 17°10′–17°40′S, from a study of Layer 2A geometry, *J. Geophys. Res.*, *102*, 10,165–10,184.

Christeson, G. L., G. M. Purdy, and G. J. Fryer (1992), Structure of young upper crust at the East Pacific Rise near 9°30′N, *Geophys. Res. Lett.*, *19*, 1045–1048.

Christeson, G. L., G. M. Purdy, and G. J. Fryer (1994), Seismic constraints on shallow crustal emplacement processes at the fast spreading East Pacific Rise, *J. Geophys. Res.*, *99*, 17,957–17,973.

Christeson, G. L., G. M. Kent, G. M. Purdy, and R. S. Detrick (1996), Extrusive thickness variability at the East Pacific Rise, 9°–10°N: Constraints from seismic techniques, *J. Geophys. Res.*, *101*, 2859–2873.

Christeson, G. L., K. D. McIntosh, and J. A. Karson (2007), Inconsistent correlation of seismic layer 2a and lava layer thickness in oceanic crust, *Nature*, *445*, 418–421, doi:10.1038/nature05517.

Cochran, J. R., D. J. Fornari, B. J. Coakley, R. Herr, and M. A. Tivey (1999), Continuous near-bottom gravity measurements made with a BGM-3 gravimeter in DSV *Alvin* on the East Pacific Rise crest near 9°31′N and 9°50′N, *J. Geophys. Res.*, *104*, 10,841–10,861.

Cowen, J. P., et al. (2007), Volcanic eruptions at East Pacific Rise near 9°50′N, *Eos Trans. AGU*, *88*(7), 81.

Detrick, R. S., P. Buhl, E. Vera, J. Mutter, J. Orcutt, J. Madsen, and T. Brocher (1987), Multi-channel seismic imaging of a crustal magma chamber along the East Pacific Rise, *Nature*, *326*, 35–41.

Dunn, R. A., D. R. Toomey, and S. C. Solomon (2000), Three-dimensional seismic structure and physical properties of the crust and shallow mantle beneath the East Pacific Rise at 9°30′N, *J. Geophys. Res.*, *105*(B10), 23,537–23,555.

Escartín, J., S. A. Soule, D. J. Fornari, M. A. Tivey, H. Schouten, and M. R. Perfit (2007), Interplay between faults and lava flows in construction of the upper oceanic crust: The East Pacific Rise crest 9°25′–9°58′N, *Geochem. Geophys. Geosyst.*, *8*, Q06005, doi:10.1029/2006GC001399.

Fornari, D. J., R. M. Haymon, M. R. Perfit, T. K. P. Gregg, and M. H. Edwards (1998), Axial summit trough of the East Pacific Rice 9°–10°N: Geological characteristics and evolu-

tion of the axial zone on fast spreading mid-ocean ridge, *J. Geophys. Res.*, *103*, 9827–9855.

Fornari, D. J., et al. (2004), Submarine lava flow emplacement at the East Pacific Rise 9°50′N: Implications for uppermost crust stratigraphy and hydrothermal fluid circulation, in *The Thermal Structure of the Ocean Crust and the Dynamics of Hydrothermal Circulation*, *Geophys. Monogr. Ser.*, vol. 148, pp. 187–217, AGU, Washington, D. C.

Garry, W. B., T. K. P. Gregg, S. A. Soule, and D. J. Fornari (2006), Formation of submarine lava channel textures: Insights from laboratory simulations, *J. Geophys. Res.*, *111*, B03104, doi:10.1029/2005JB003796.

Gee, J., and D. V. Kent (1994), Variations in Layer 2a thickness and the origin of the central anomaly magnetic high, *Geophys. Res. Lett.*, *21*, 297–300.

Gee, J., and D. V. Kent (1997), Magnetization of axial lavas from the southern East Pacific Rise (14°–23°S): Geochemical controls on magnetic properties, *J. Geophys. Res.*, *102*, 24,873–24,886.

Gee, J., D. A. Schneider, and D. V. Kent (1996), Marine magnetic anomalies as recorders of geomagnetic intensity variations, *Earth Planet. Sci. Lett.*, *144*, 327–335.

Gee, J., S. C. Cande, J. A. Hildebrand, K. Donnelly, and R. L. Parker (2000), Geomagnetic intensity variations over the past 780 kyr obtained from near-seafloor magnetic anomalies, *Nature*, *408*, 827–832.

Goldstein, S. J., M. R. Perfit, R. Batiza, D. J. Fornari, and M. T. Murrell (1994), Off-axis volcanism at the East Pacific Rise detected by uranium-series dating of basalts, *Nature*, *367*, 157–159.

Gregg, T. K. P., and J. H. Fink (1995), Quantification of submarine lava flow morphology through analog experiments, *Geology*, *23*, 73–76.

Gregg, T. K. P., D. J. Fornari, M. R. Perfit, R. M. Haymon, and J. H. Fink (1996), Rapid emplacement of a mid-ocean ridge lava flow on the East Pacific Rise at 9°46′–51′N, *Earth Planet. Sci. Lett.*, *144*, E1–E7.

Guspi, F. (1987), Frequency-domain reduction of potential field measurements to a horizontal plane, *Geoexploration*, *24*, 87–98.

Guyodo, Y., and J. Valet (1999), Global changed in intensity of the Earth's magnetic field during the past 800 kyr, *Nature*, *399*, 247–252.

Harding, A. J., G. M. Kent, and J. A. Orcutt (1993), A multichannel seismic investigation of upper crustal structure at 9°N on the East Pacific Rise: Implications for crustal accretion, *J. Geophys. Res.*, *98*, 13,925–13,944.

Haymon, R. M., and S. M. White (2004), Fine-scale segmentation of volcanic/hydrothermal systems along fast-spreading ridge crests, *Earth Planet. Sci. Lett.*, *226*, 367–382.

Haymon, R. M., D. J. Fornari, M. H. Edwards, S. Carbotte, D. Wright, and K. C. Macdonald (1991), Hydrothermal vent distribution along the East Pacific Rise crest (9°09′–54′N) and its relationship to magmatic and tectonic processes on fast-spreading mid-ocean ridges, *Earth Planet. Sci. Lett.*, *104*, 513–534.

Haymon, R. M., et al. (1993), Volcanic eruption of the mid-ocean ridge along the East Pacific Rise crest at 9°45′–53′N: Direct submersible observations of seafloor phenomenon associated with an eruption event in April, 1991, *Earth Planet. Sci. Lett.*, *119*, 85–101.

Hooft, E. E. E., H. Schouten, and R. S. Detrick (1996), Constraining crustal emplacement processes from the variation in seismic layer 2A thickness at the East Pacific Rise, *Earth Planet. Sci. Lett.*, *142*, 289–309.

IAGA Division V Working Group (2000), International geomagnetic reference field 2000, *Geophys. J. Int.*, *141*, 256–262.

Irving, E. (1970), The Mid-Atlantic Ridge at 45°N, XIV, Oxidation and magnetic properties of basalts; review and discussion, *Can. J. Earth Sci.*, *7*, 1528–1538.

Isezaki, N. (1986), A new shipboard three-component magnetometer, *Geophysics*, *51*, 1992–1998.

Johnson, H. P., and M. A. Tivey (1995), Magnetic properties of zero-age oceanic crust: A new submarine lava flow on the Juan de Fuca Ridge, *Geophys. Res. Lett.*, *22*, 175–178.

Karson, J. A. (1998), Internal structure of oceanic lithosphere: A perspective from tectonic windows, in *Faulting and Magmatism at Mid-Ocean Ridges*, *Geophys. Monogr. Ser.*, vol. 106, edited by W. R. Buck et al., pp. 177–218, AGU, Washington, D. C.

Karson, J. A., S. D. Hurst, and P. Lonsdale (1992), Tectonic rotations of dikes in fast-spreading oceanic crust exposed near Hess Deep, *Geology*, *20*, 685–688.

Karson, J. A., M. A. Tivey, and J. R. Delaney (2002), Internal structure of uppermost oceanic crust along the Western Blanco Transform Scarp: Implications for subaxial accretion and deformation at the Juan de Fuca Ridge, *J. Geophys. Res.*, *107*(B9), 2181, doi:10.1029/2000JB000051.

Kent, G. M., A. J. Harding, and J. A. Orcutt (1993), Distribution of magma beneath the East Pacific Rise near the 9°03′N overlapping spreading center from forward modeling of common depth point data, *J. Geophys. Res.*, *98*, 13,971–13,995.

Kidd, R. G. W. (1977), A model for the process of formation of the upper oceanic crust, *Geophys. J R. Astron. Soc.*, *50*, 149–183.

Klitgord, K. D. (1976), Sea-floor spreading: The central anomaly magnetization high, *Earth Planet. Sci. Lett.*, *29*, 201–209.

Klitgord, K. D., and J. Mammerickx (1982), Northern East Pacific Rise: Magnetic anomaly and bathymetric framework, *J. Geophys. Res.*, *87*, 6725–6750.

Korenaga, J. (1995), Comprehensive analysis of marine magnetic vector anomalies, *J. Geophys. Res.*, *100*, 365–378.

Kurras, G. J., D. J. Fornari, M. H. Edwards, M. R. Perfit, and M. C. Smith (2000), Volcanic morphology of the East Pacific Rise crest 9°49′–52′N: Implications for volcanic emplacement processes at fast-spreading mid-ocean ridges, *Mar. Geophys. Res.*, *21*, 23–41.

Lagabrielle, Y., D. Bideau, M. Cannat, J. A. Karson, and C. Mével (1998), Ultramafic-mafic plutonic rock suites along the Mid-Atlantic Ridge (10°N–30°N): Symmetrical distribution and implications for seafloor spreading processes, in *Faulting and Magmatism at Mid-Ocean Ridges*, *Geophys. Monogr. Ser.*, vol. 106, edited by W. R. Buck et al., pp. 153–176, AGU, Washington, D. C.

Langmuir, C. H., J. F. Bender, and R. Batiza (1986), Petrological and tectonic segmentation of the East Pacific Rise, 5°30′–14°30′N, *Nature*, *322*, 422–429.

Lee, S. M., S. C. Solomon, and M. A. Tivey (1996), Fine-scale crustal magnetization variations and segmentation of the East Pacific Rise, 9°10′–9°50′N, *J. Geophys. Res.*, *101*, 22,033–22,050.

Lonsdale, P. (1983), Overlapping rift zones at the 5.5°S offset of the East Pacific Rise, *J. Geophys. Res.*, *88*, 9393–9406.

Macdonald, K. C., and P. J. Fox (1983), Overlapping spreading centers: New accretion geometry on the East Pacific Rise, *Nature*, *301*, 55–58.

Macdonald, K. C., and P. J. Fox (1988), The axial summit graben and cross-sectional shape of the East Pacific Rise

as indicators of axial magma chambers and recent volcanic eruptions, *Earth Planet. Sci. Lett.*, *88*, 119–131.

Macdonald, K. C., S. P. Miller, S. P. Huestis, and F. N. Spiess (1980), Three-dimensional modeling of a magnetic reversal boundary from inversion of deep-tow measurements, *J. Geophys. Res.*, *85*, 3670–3680.

Macdonald, K. C., S. P. Miller, B. P. Luyendyk, T. M. Atwater, and L. Shure (1983), Investigation of a Vine-Matthews magnetic lineation from a submersible: The source and character of marine magnetic anomalies, *J. Geophys. Res.*, *88*, 3403–3418.

Macdonald, K. C., J.-C. Sempere, and P. J. Fox (1984), East Pacific Rise from Siqueiros to Orozo Fracture Zones: Along-strike continuity of axial neovolcanic zone and structure and evolution of overlapping spreading center, *J. Geophys. Res.*, *89*, 6049–6069.

Macdonald, K. C., J.-C. Sempere, P. J. Fox, and R. Tyce (1987), Tectonic evolution of ridge-axis discontinuities by the meeting, linking, or self decapitation of neighboring ridge segments, *Geology*, *15*, 993–997.

Macdonald, K. C., P. J. Fox, L. J. Perram, M. F. Eisen, R. M. Haymon, S. P. Miller, S. M. Carbotte, M.-H. Cormier, and A. N. Shor (1988), A new view of the mid-ocean ridge from the behaviour of ridge axis discontinuities, *Nature*, *335*, 217–225.

Macdonald, K. C., D. S. Scheirer, and S. C. Carbotte (1991), Mid-ocean ridges: Discontinuities, segments and giant cracks, *Science*, *253*, 986–994.

Macdonald, K. C., et al. (1992), The East Pacific Rise and its flanks, 8°–18°N: History of segmentation, propagation and spreading direction based on SeaMARC II and Sea Beam studies, *Mar. Geophys. Res.*, *14*, 299–344.

Marshall, M., and A. Cox (1971), Magnetism of pillow basalts and their petrology, *Geol. Soc. Am. Bull.*, *82*, 537–552.

Pariso, J. E., and H. P. Johnson (1991), Alteration processes at Deep Sea Drilling Project/Ocean Drilling Program Hole 504B at the Coast Rica Rift, *J. Geophys. Res.*, *96*, 11,703–11,722.

Parker, R. L., and S. P. Huestis (1974), The inversion of magnetic anomalies in the presence of topography, *J. Geophys. Res.*, *79*, 1587–1594.

Perfit, M. R., and J. W. W. Chadwick (1998), Magmatism at mid-ocean ridges: Constraints from volcanological and geochemical investigations, in *Faulting and Magmatism at Mid-Ocean Ridges*, *Geophys. Monogr. Ser.*, vol. 106, edited by W. R. Buck et al., pp. 57–115, AGU, Washington, D. C.

Perfit, M. R., D. J. Fornari, and M. C. Smith (1994), Small-scale spatial and temporal variations in mid-ocean ridge crest magmatic processes, *Geology*, *22*, 375–379.

Prevot, M., and A. Lecaille (1976), Comments on paper by K. D. Klitgord, "Sea-floor spreading: The central anomaly magnetization high," *Earth Planet. Sci. Lett.*, *33*, 164–168.

Reynolds, J. R., and C. H. Langmuir (2000), Identification and implications of off-axis lava flows around the East Pacific Rise, *Geochem. Geophys. Geosyst.*, *1*(6), doi:10.1029/1999GC000033.

Rubin, K. H., J. D. Macdougall, and M. R. Perfit (1994), $^{210}$Po-$^{210}$Pb dating of recent volcanic eruptions on the sea floor, *Nature*, *368*, 841–844.

Scheirer, D. S., D. J. Fornari, S. E. Humphris, and S. Lerner (2000), High-resolution seafloor mapping using the DSL-120 sonar system: Quantitative assessment of sidescan and phase-bathymetry data from the Lucky Strike segment of the Mid-Atlantic Ridge, *Mar. Geophys. Res.*, *21*, 121–142.

Schouten, H., and R. Denham (1979), Modeling the oceanic magnetic source layer, in *Deep Drilling Results in the Atlantic Ocean: Continental Margins and Paleoenvironment*, *Maurice Ewing Ser.*, vol. 3, edited by M. Talwani et al., pp. 151–159, AGU, Washington, D. C.

Schouten, H., M. A. Tivey, D. J. Fornari, and J. R. Cochran (1999), Central anomaly magnetization high: Constraints on the volcanic construction and architecture of seismic layer 2A at a fast-spreading mid-ocean ridge, the EPR at 9°30′–50′N, *Earth Planet. Sci. Lett.*, *169*, 37–50.

Schouten, H., M. Tivey, D. Fornari, D. Yoerger, A. Bradley, M. Edwards, and P. Johnson (2003), Central Anomaly Magnetization High: Constraints on the volcanic construction and architecture of young upper oceanic crust, EPR 9°–10°N, *Ridge 2000 Events*, *1*(1), 30–34.

Sempere, J.-C., K. C. Macdonald, and S. P. Miller (1984), Overlapping spreading centres: 3-D inversion of the magnetic field at 9°03′N on the East Pacific Rise, *Geophys. J. Int.*, *79*, 799–811.

Sempere, J.-C., A. Meshkov, M. Thommeret, and K. C. Macdonald (1988), Magnetic properties of some young basalts from the East Pacific Rise, *Mar. Geophys. Res.*, *9*, 131–146.

Sims, K. W. W., et al. (2002), Chemical and isotropic constraints on the generation and transport of magma beneath the East Pacific Rise, *Geochim. Cosmochim. Acta*, *66*(19), 3481–3504.

Smith, G. M., and S. K. Banerjee (1986), Magnetic structure of the upper kilometer of the marine crust at Deep Sea Drilling Project hole 504B, eastern Pacific Ocean, *J. Geophys. Res.*, *91*, 10,337–10,354.

Smith, M. C., M. R. Perfit, D. J. Fornari, W. I. Ridley, M. H. Edwards, G. J. Kurras, and K. L. Von Damm (2001), Magmatic processes and segmentation at a fast spreading mid-ocean ridge: Detailed investigation of an axial discontinuity on the East Pacific Rise crest at 9°37′N, *Geochem. Geophys. Geosyst.*, *2*(10), doi:10.1029/2000GC000134.

Sohn, R. A., and K. W. W. Sims (2005), Bending as a mechanism for triggering off-axis volcanism on the East Pacific Rise, *Geology*, *33*(93–96).

Soule, S. A., D. J. Fornari, M. R. Perfit, M. A. Tivey, W. I. Ridley, and H. Schouten (2005), Channelized lava flows at the East Pacific Rise crest 9°–10°N: The importance of off-axis lava transport in developing the architecture of young oceanic crust, *Geochem. Geophys. Geosyst.*, *6*, Q08005, doi:10.1029/2005GC000912.

Soule, S. A., et al. (2007), New insights into mid-ocean ridge volcanic processes from the 2005–2006 eruption of the East Pacific Rise, 9°46′N–9°56′N, *Geology*, *35*, 1079–1082.

Tivey, M. A. (1996), Vertical magnetic structure of ocean crust determined from near-bottom magnetic field measurements, *J. Geophys. Res.*, *101*, 20,275–20,296.

Tivey, M. A., and H. P. Johnson (1987), The central anomaly magnetic high: Implications for ocean crust construction and evolution, *J. Geophys. Res.*, *92*, 12,685–12,694.

Tivey, M. A., and H. P. Johnson (1993), Variations in oceanic crustal structure and implications for the fine scale magnetic anomaly signal, *Geophys. Res. Lett.*, *20*, 1879–1882.

Tolstoy, M., et al. (2006), A sea-floor spreading event captured by seismometers, *Science*, *314*, 1920–1922.

Toomey, D. R., G. M. Purdy, S. C. Solomon, and W. S. D. Wilcock (1990), The three-dimensional seismic velocity structure of the East Pacific Rise near latitude 9°30′N, *Nature*, *347*, 639–645.

Toomey, D. R., S. C. Solomon, and G. M. Purdy (1994), Tomographic imaging of the shallow crustal structure of the East Pacific Rise at 9°30′N, *J. Geophys. Res.*, *99*, 24,135–24,157.

Vera, E. E., and J. B. Diebold (1994), Seismic imaging of oceanic layer 2A between 9°30′N and 10°N on the East

Pacific Rise from two-ship wide-aperture profiles, *J. Geophys. Res.*, *99*, 3031–3041.

White, S. M., R. Haymon, D. J. Fornari, M. R. Perfit, and K. C. Macdonald (2002), Correlation between volcanic and tectonic segmentation of fast spreading ridges: Evidence from volcanic structures and lava flow morphology on the East Pacific Rise at 9°–10°N, *J. Geophys. Res.*, *107*(B8), 2173, doi:10.1029/2001JB000571.

White, S. M., R. M. Haymon, and S. Carbotte (2006), A new view of ridge segmentation and near-axis volcanism at the East Pacific Rise, 8°–12°N, from EM300 multibeam bathymetry, *Geochem. Geophys. Geosyst.*, *7*, Q12O05, doi:10.1029/2006GC001407.

Wilson, D. S., et al. (2006), Drilling to gabbro in intact ocean crust, *Science*, *312*(5776), 1016–1020.

Wright, D. J., R. M. Haymon, and D. J. Fornari (1995), Crustal fissuring and its relationship to magmatic and hydrothermal processes on the East Pacific Rise crest (9°12′ to 54′N), *J. Geophys. Res.*, *100*, 6097–6120.

Yang, S., H. Odah, and J. Shaw (2000), Variations in the geomagnetic dipole moment over the last 12000 years, *Geophys. J. Int.*, *140*, 158–162.

Yoerger, D., et al. (1996), Near-bottom magnetic survey of the Coaxial Ridge segment using the Autonomous Benthic Explorer survey vehicle, *RIDGE Events*, *7*, 5–9.

Zhou, W., R. Van der Voo, and D. R. Peacor (1997), Single-domain and superparamagnetic titanomagnetite with variable Ti content in young ocean-floor basalts: No evidence for rapid alteration, *Earth Planet. Sci. Lett.*, *150*, 353–362.